J. Fluid Mech. (1992), *vol.* 244, *pp.* 677–712

Copyright © 1992 Cambridge University Press

Direct simulation of the stably stratified turbulent Ekman layer

By G. N. COLEMAN[1]†, J. H. FERZIGER[1] AND P. R. SPALART[2]‡
[1] Department of Mechanical Engineering, Stanford University, Stanford, CA 94305, USA
[2] NASA Ames Research Center, Moffett Field, CA 94035, USA

(Received 15 August 1991 and in revised form 16 May 1992)

The three-dimensional time-dependent turbulent flow in the stably stratified Ekman layer over a smooth surface is computed numerically by directly solving the Navier–Stokes equations, using the Boussinesq approximation to account for buoyancy effects. All relevant scales of motion are included in the simulation so that no turbulence model is needed. The Ekman layer is an idealization of the Earth's boundary layer and provides information concerning atmospheric turbulence models. We find that, when non-dimensionalized according to Nieuwstadt's local scaling scheme, some of the simulation data agree very well with atmospheric measurements. The results also suggest that Brost & Wyngaard's 'constant Froude number' and Hunt's 'shearing length' stable layer models for the dissipation rate of turbulent kinetic energy are both valid, when Reynolds number effects are accounted for. Simple gradient closures for the temperature variance and heat flux demonstrate the same variation with Richardson number as in Mason & Derbyshire's large-eddy simulation (LES) study, implying both that the models are relatively insensitive to Reynolds number and that local scaling should work well when applied to the stable atmospheric layer. In general we find good agreement between the direct numerical simulation (DNS) results reported here and Mason & Derbyshire's LES results.

1. Introduction

Ekman (1905) was the first to analyse the effect of system rotation on the boundary layer that came to bear his name. Although he considered only the shear-driven layer, Ekman's analysis also applies to flow driven by a mean pressure gradient. The stably stratified turbulent pressure-driven Ekman layer – an idealization of the Earth's nocturnal boundary layer – is the focus of the present study. This paper is an extension of the analysis of the unstratified Ekman layer described in Coleman, Ferziger & Spalart (1990*a*, hereinafter referred to as CFS*a*).

Buoyancy can dramatically alter the structure of a turbulent flow, including that within the atmosphere adjacent to the Earth's surface, the planetary boundary layer (PBL). When this turbulence is vigorously heated from below or cooled from above, the large-scale motions that result greatly increase the rate of transport relative to that found in the neutrally stratified layer with the same free-stream wind speed. The patterns formed by the buoyancy-induced motions are often quite coherent. They can range from 'Bénard cells' to 'longitudinal rolls'. The former are present when the

---

† Present address: NASA Ames Research Center, Moffett Field, CA 94035, USA.
‡ Present address: Boeing Commercial Airplane Group, PO Box 3707, Seattle, WA 98124, USA.

buoyant forcing is much more important than the forcing due to shear, and the latter when the two effects are comparable (LeMone 1973; Schmidt & Schumann 1989; Coleman, Ferziger & Spalart 1990*b*, hereinafter referred to as CFS*b*). Both are associated with striking cloud formations: 'convection rings' and 'cloud streets', respectively.

For the stably stratified (which we shall term the 'stable') layer considered here, buoyancy leads to important, although more subtle, modifications of the flow. By diminishing the vertical velocity fluctuations, a buoyantly stable temperature profile reduces the ability of the turbulence to transport momentum, heat and contaminants vertically, and may lead to the total collapse of the turbulent state (Turner 1973). Between the extremes of the fully turbulent and relaminarized states, the stable PBL can exhibit a number of phenomena. These include enhanced anisotropy and intermittency of the turbulence and the creation of internal (buoyancy) waves (with possible nonlinearity and breaking). When the terrain is complicated, buoyant stability can cause both large-scale internal 'mountain' waves and 'drainage' flows; very small changes in the slope of the terrain can profoundly influence the layer (Brost & Wyngaard 1978). In addition, stable stratification is generally associated with transient behaviour, so history effects are often important.

All of these effects must be correctly accounted for by parameterizations of the stably stratified PBL, which are used in climate and weather predictions, dispersion studies, and civil engineering design projects. In this paper we restrict our attention to a simple model of the stable PBL: the stably stratified turbulent Ekman layer. That is, we examine the turbulent flow of a viscous fluid over a cooled smooth flat surface, driven by a uniform horizontal pressure gradient while experiencing steady system rotation about a vertical axis in a vertically oriented gravitational field. Consequently, the effects of moisture, radiation and terrain (and latitude – see CFS*a*) are neglected so that we can concentrate on the interaction of the turbulence with the stratification. The resulting insight can then be used to evaluate, and hopefully improve upon, stable-layer parameterizations.

To achieve this goal, we shall rely upon numerical simulations of the unsteady three-dimensional details of the turbulence. We choose to employ the technique of direct numerical simulation (DNS) and resolve all of the relevant scales of motion, so that no subgrid-scale model is required. Unlike large-eddy simulation (LES), DNS produces results that are free from modelling errors. These errors are especially important near the surface. Owing to computer limitations, however, we are restricted to very low, meteorologically unrealistic, Reynolds numbers that are of the order of 10^2. Since atmospheric Reynolds numbers can be as large as 10^8 (Wyngaard 1992), generalization of our findings to the PBL must be made with care. The focus will be upon Reynolds-number-independent behaviour insofar as possible.

DNS investigations of stably stratified turbulence have also been performed by Riley, Metcalfe & Weissman (1981), Gerz, Schumann & Elghobashi (1989) and Holt, Koseff & Ferziger (1992), all for the case of homogeneous shear flow. The work most closely related to that presented here, however, is the LES study of the stable PBL done by Mason & Derbyshire (1990). Although there are differences in the flows considered (for example, different Reynolds numbers and stratification profiles), the results will be compared when it is useful to do so.

The specific goals of this study are to discern the 'structural' differences between the turbulence in the neutrally and stably stratified Ekman layers (by comparing, for example, eddy size and shape, and vertical profiles of Reynolds-averaged statistics), and to evaluate some parameterizations recommended for use in stable PBLs (we shall consider the Reynolds-averaged closures of Brost & Wyngaard 1978, Nieuwstadt 1984, Hunt, Kaimal & Gaynor 1985 and Hunt, Stretch & Bitter 1988). A secondary benefit (as with CFS*a*) will be the demonstration of the advantages and limitations of using DNS as an atmospheric-turbulence research tool.

In the next section, the governing equations and a detailed description of the flow are presented. A summary of the numerical method employed is given in §3. The parameters for each of the DNS runs are listed in §4. Sections 5 and 6 contain the simulation results, and §7 the discussion and conclusions.

2. Problem formulation and flow description

The equations to be solved are those that govern the flow of a thermally stratified viscous fluid, driven by a uniform pressure gradient and experiencing steady system rotation. The Boussinesq approximation is used to account for the buoyancy of the fluid; that is, density variations are assumed to have no dynamic influence other than to provide a temperature-dependent body force. The equation set is thus

$$\frac{\partial \boldsymbol{u}}{\partial t}+\boldsymbol{u}\cdot\nabla\boldsymbol{u} = -\frac{1}{\rho_\infty}\nabla p+2\boldsymbol{\Omega}\times(\boldsymbol{G}-\boldsymbol{u})-\Phi\boldsymbol{g}+\nu\nabla^2\boldsymbol{u}, \tag{1}$$

$$\nabla\cdot\boldsymbol{u} = 0, \tag{2}$$

$$\frac{\partial \Phi}{\partial t}+\nabla\cdot(\boldsymbol{u}\Phi) = \kappa\nabla^2\Phi. \tag{3}$$

Here, $\boldsymbol{\Omega}$ is the vertically oriented angular velocity of the system, and $\boldsymbol{G}$ is the (horizontal) geostrophic wind that defines, along with the acceleration due to gravity vector $\boldsymbol{g}$, the imposed uniform pressure gradient via

$$\nabla P = -2\rho_\infty\boldsymbol{\Omega}\times\boldsymbol{G}+\rho_\infty\boldsymbol{g}. \tag{4}$$

The variable p is the deviation of the pressure from the imposed field given by (4), $\boldsymbol{u}$ the velocity vector, ρ_∞ the reference fluid density (all reference quantities are taken to be the value of the quantity observed as the elevation $z\rightarrow\infty$) and ν and κ the kinematic viscosity and thermal diffusivity, respectively, both of which are assumed to be constant. The non-dimensional temperature, Φ, is defined as

$$\Phi \equiv (T-T_\infty)/T_\infty, \tag{5}$$

where T and T_∞ are the local and reference temperatures. To differentiate between adiabatic and diabatic temperature changes – since in the PBL only the latter produces a net buoyant forcing – T represents not the actual, but the potential temperature (Holton 1979). (The hydrostatic pressure variation over the depth of the PBL is small, so the difference between the two is slight (Businger 1982).)

The momentum, continuity and temperature equations are solved over the semi-infinite Cartesian domain above a smooth flat surface (with the z-axis directed vertically upward, and the x-axis parallel to $\boldsymbol{G}$): $-\infty\leqslant x\leqslant\infty$, $-\infty\leqslant y\leqslant\infty$, $0\leqslant z\leqslant\infty$, subject to the boundary conditions

$$\boldsymbol{u}=0 \quad\text{at}\quad z=0, \qquad \boldsymbol{u}\rightarrow\boldsymbol{G} \quad\text{as}\quad z\rightarrow\infty, \tag{6a}$$

$$\Phi=\Phi_0 \quad\text{at}\quad z=0, \qquad \Phi\rightarrow 0 \quad\text{as}\quad z\rightarrow\infty. \tag{6b}$$

We choose an isothermal (rather than, say, constant heat flux or constant cooling rate) lower boundary condition, with Φ_0 the lowest temperature in the layer. In

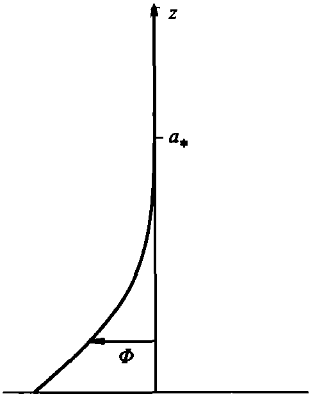

FIGURE 1. Initial stable temperature profile. $\Phi = (T - T_\infty)/T_\infty$.

contrast to the unstratified counterpart (cf. CFS*a*), a state of statistical equilibrium does not exist in the cooled layer, since the temperature profile (and therefore its slope) cannot be independent of time without a heat source within the domain. A type of 'quasi-equilibrium' is possible if the turbulence adjusts very quickly to changes in the mean velocity and temperature profiles, but the mean flow is time dependent. The initial conditions and time are therefore parameters that specify the flow state. The others are the thermal diffusivity of the fluid, κ, the reference temperature, T_∞, the surface temperature, Φ_0, the acceleration due to gravity, g, as well as the parameters that also apply to the neutrally stratified (which we shall term the 'neutral') Ekman layer: the magnitude of the system rotation Ω, the kinematic viscosity, ν, and the geostrophic wind speed, G. In CFS*a*, variations in latitude and the direction of $\boldsymbol{G}$ were found to be important; these are excluded in the present flow, however, since $\boldsymbol{\Omega}$ is allowed no horizontal component.

The velocity initial conditions are from one of the fully developed, statistically stationary, unstratified turbulent fields of CFS*a*. The initial temperature field varies only in z. (There is evidence (Hunt *et al.* 1988; Gerz *et al.* 1989) that in stably stratified flows the temperature history may be sensitive to initial conditions, in that temperature fields that contain initial fluctuations can develop smaller oscillations than initial fields that are disturbance free.) A common feature of boundary layers that are cooled from below (as opposed to heated from above) is that the maximum of the temperature gradient, $\Gamma = \mathrm{d}\langle T\rangle/\mathrm{d}z$ (i.e. the lapse rate), is found at the surface (Wyngaard 1983). Within the limits imposed by this constraint, a variety of temperature profiles is observed. Idealizations with linear, polynomial and exponential variations of $T(z)$ have been proposed (Stull 1988). In this study, we utilize an error-function initial temperature profile, so that Γ is maximum at $z = 0$ and decreases monotonically with increasing elevation. The initial (potential) temperature profile, shown in figure 1, is thus

$$T(z) = \frac{a_*}{2}\left(\frac{-\pi}{\ln(0.01)}\right)^{\frac{1}{2}} \Gamma_{0,0}\,\mathrm{erf}\left(\frac{z/a_*}{(-\ln(0.01))^{-\frac{1}{2}}}\right) + T_0, \tag{7}$$

where erf is the error function, $\Gamma_{0,0}$ is the initial surface lapse rate, T_0 is the surface temperature (which is held fixed) and a_* is the height at which $\mathrm{d}T/\mathrm{d}z$ is 1 % of $\Gamma_{0,0}$. (A single zero subscript, as on T_0, is used throughout to indicate the value of a quantity at the *surface*, while a double zero subscript, such as on $\Gamma_{0,0}$, denotes a *surface* quantity at the *beginning* of a simulation.) The parameters that characterize the initial T distribution are thus $\Gamma_{0,0}$ and the lengthscale a_*. When a_* is small, $T(z)$ typifies the early evening profile over land, just after the transition from convective (or neutral) to stable conditions. Large a_* is characteristic of late night and early morning over land, when the effect of surface cooling has propagated to higher elevations. The profile (7) will be imposed upon a fully developed turbulent neutral field, after which the mean temperature will evolve in a manner determined by the time-dependent (since T_0 is fixed) surface heat flux, Q_0, and the dynamics of the resulting turbulence.

From the above, we see that a relevant set of non-dimensional flow parameters includes a Reynolds number,

$$Re \equiv GD/\nu = G/(\nu f/2)^{\frac{1}{2}}$$

(f is the Coriolis parameter, here equal to 2Ω, and D is the laminar Ekman layer depth, $D = (2\nu/f)^{\frac{1}{2}}$); an initial surface Richardson number,

$$Ri_{0,0} \equiv g\Gamma_{0,0}D^2/(T_\infty G^2);$$

the Prandtl number, $Pr \equiv \nu/\kappa$; the non-dimensional initial thermal lengthscale a_*/D; and the non-dimensional time tf. This parameter set will be used to define each DNS.

3. Numerical method

The weighted-residual method described by Spalart, Moser & Rogers (1991) is used to compute solutions of (1)–(3). The technique utilizes basis functions that satisfy the continuity equation and the boundary conditions. This results in solving, instead of an initial-boundary-value problem, a set of coupled ordinary differential equations without constraints. The method is spectrally accurate (that is, the numerical error approaches zero faster than any power of the grid spacing as the resolution is increased) in all three spatial directions, and second-order accurate in time. Those interested in more details than are presented in the following overview are referred to CFS*b* or Spalart *et al.* (1991).

Each of the dependent variables is assumed to exhibit periodic variations of finite wave-length in the directions parallel to the surface, and is represented by Fourier series in x and y. Provided the wavelength is sufficiently larger than any large-scale flow feature, this allows the infinite-domain solution to be simulated on a domain of finite horizontal extent. Mass is exactly conserved at each point of the simulation; the divergence-free nature of the velocity fields is built into the basis functions by defining the basis functions such that the three Fourier-transformed components of the velocity field satisfy (2) at each (two-dimensional) wavevector $\boldsymbol{k}$. This leads naturally to solving a Galerkin weak formulation of the momentum equation (also known as the Leray formulation). The basis and weight functions are the same, and thus both satisfy the boundary conditions.

This formulation removes the need to explicitly compute the pressure field to determine the velocity, and reduces the number of dependent variables by two (the pressure and one velocity component are eliminated). In the z-direction, the velocity and temperature are approximated by finite series of M_z polynomials in an exponentially mapped vertical coordinate, $\zeta = \exp(-z/Z)$, where Z is the mapping lengthscale. The polynomials in ζ consist of a family of Jacobi polynomials (Abramowitz & Stegun 1972) multiplied by low-order polynomials (for example

$\zeta(1-\zeta)$) in order to guarantee that the dependent variables satisfy the boundary conditions at the top and bottom of the domain. With the proper choice of Z, the use of the exponential mapping and Jacobi polynomials has been found to provide an efficient scheme for resolving turbulent boundary layers (Spalart 1988, 1989). Each velocity basis function contains a term that exactly represents the slowly decaying irrotational velocity fluctuations. This allows the vertical grid points to be clustered in the highly vortical region near the surface, without compromising accuracy in the outer flow. Since complex exponentials and Jacobi polynomials can both represent smooth functions to spectral accuracy, the method is also expected to very accurately represent solutions to the Navier–Stokes equations. (Although no formal proof of this has been found, very rapid convergence is found in practice (see Spalart *et al.* 1991).)

This spatial discretization produces, for each $\boldsymbol{k}$, three (two for velocity, one for temperature) sets of M_z coupled ordinary differential equations for the unknown Jacobi expansion coefficients, and converts the mixed initial-boundary-value problem to a pure initial-value problem. The orthogonality of the Jacobi polynomials produces matrices of narrow band-width, an attribute that reduces the cost of the computation. To solve the equation sets, a mixed Runge–Kutta (third-order)/Crank–Nicolson time-advance algorithm is employed. Because the Crank–Nicolson integration is second order, the algorithm is formally second order in time, with the higher-order Runge–Kutta accuracy apparently wasted. However, since the maximum allowable step size is determined by the numerical stability requirements of the explicit scheme (which is applied to the nonlinear, Boussinesq, and Coriolis terms), and the third-order Runge–Kutta method allows a larger timestep than the second-order version, there is an advantage to mixing methods of different order. This is especially true when numerical stability requires the same timestep as numerical accuracy. To increase the allowable timestep, the integration is performed in a translating Galilean reference frame moving in the x-direction at half the free-stream geostrophic velocity. To avoid 'aliasing' numerical errors during the integration of the nonlinear terms, the number of collocation points (N_x, N_y, N_z) is 50% greater than the number of expansion coefficients in each of the spatial directions. The most expensive parts of the method are the 'Jacobi transforms' to and from polynomial space, which typically require 40% of the CPU time; the operation count for these transforms at each Runge–Kutta substep is $33 M_x \times M_y \times M_x^2$, where M_x, M_y and M_z are the number of expansion coefficients in the x-, y- and z-directions.

The accuracy of the code that uses the above method was verified by computing the growth rates and phase speeds of linear instabilities in the neutrally, stably and unstably stratified laminar Ekman layer. In all cases, excellent agreement was found between the reference values and those produced by the code (see CFS*b*). This agreement, along with Spalart's (1988, 1989) previous success using the algorithm for non-rotating, unstratified turbulent boundary layers, provides the basis for our confidence in the DNS results that follow.

A further test of numerical accuracy was made at a referee's request for an assessment of the method's ability to conserve momentum and energy. These findings also apply to other simulations that use the present method, at least qualitatively. The method does not provide for exact conservation of global momentum or kinetic energy. Such conservation is sometimes achieved, through cancellation of local errors. As discussed by Spalart *et al.* (1991, p. 307) the method has the property of 'semi-conservation' of energy (Gottlieb & Orszag 1977), save for a contribution due to the surface and free-stream boundary conditions (in the notation of Spalart *et al.* (1991), the '$U_0 \neq 0$' contribution) that turns out to be very small (see below). Semi-conservation means that energy would be conserved if the time integration were exact.

We found that the imbalances due to spatial discretization alone are typically 10^{-5} in the global momentum and energy budgets, normalized by D and G. In comparison, the largest terms in the global energy budget (the production and dissipation), are about 10^{-3} in those units. These imbalances are caused by the boundary-condition term mentioned above, an inexact Gauss quadrature of a cross-term between the polynomials and the irrotational component, and round-off errors. When the code was run with the usual value of the timestep, we found that the time discretization leads to a negligible loss of global momentum, of the order of 10^{-5} of the largest term in the budget, but causes a significant drain in the turbulent kinetic energy equation, equivalent to from about 4 to 6% of the viscous dissipation. This is consistent with the characteristics (as predicted by linear theory for advection-dominated processes) of the Runge–Kutta third-order scheme, which we use in its stable region since the CFL number is kept below $\sqrt{3}$; we thus expect the scheme to remove energy, primarily from the small turbulent scales, making the small contribution needed to close the budget. To explore this conjecture we re-ran a case with the timestep halved, with the result that the viscous dissipation approached a value that was about 4% larger than that produced by the run using the full timestep. This strongly supports the view that Runge–Kutta third-order errors slightly damp the small scales in what amounts to a numerical dissipation, since this effect 'communicates' with the true, viscous, dissipation so that the total effective dissipation remains approximately constant. (Conversely, we expect simulations with schemes such as the Adams–Bashforth algorithm, which linear theory predicts will amplify the smallest scales, to experience an increase of the small-scale energy from time-integration errors.)

In the past the precise influence of the time-discretization was not measured since the local energy budgets for stationary flows were found to balance extremely well near the surface, and any lack of balance away from the surface was attributed mostly to the lack of adequate statistical sample, and to the relative coarseness of the vertical grid. In retrospect, another probable contributor to the outer-layer imbalances is the time-discretization error, given that the largest relative differences between the full-timestep and half-timestep runs mentioned above occur in this region. In practice, this is of little consequence: a grid-refinement study, in which we estimate the time-integration errors were cut several-fold, failed to produce any sizable change in the first- and second-order statistics (Spalart 1988). The interpretation of the time-integration errors as a slight numerical dissipation is not disturbing, in that the turbulent scales it affects are also strongly affected by spatial truncation errors. Those who perform turbulent simulations must always assume that the energy-containing scales have little sensitivity to how exactly energy is removed from the smallest resolved scales, whether by true viscosity (or subgrid-scale models or 'hyper-viscosities'), or by numerical errors of the spatial or temporal kind.

4. Cases

4.1. *Physical parameters*

Two simulations, Cases SA and NSA, will be discussed in detail. They were run at the same Reynolds, Prandtl, and initial surface Richardson numbers and lengthscale ratio: $Re = 400, Pr = 0.7, Ri_{0,0} = 0.001$ and $a_*/D = 10$. The difference between these runs is that in Case NSA the density is unaffected by the temperature, so the temperature acts as a passive scalar. The value $Ri_{0,0} = 0.001$ is near the maximum that allows the flow to remain turbulent at this Reynolds number; when $Ri_{0,0} > 0.001$, the $Re = 400$ layer relaminarizes when the $a_*/D = 10$ stable temperature profile is superimposed upon the neutral flow (see CFS*b*). Results from three other turbulence-sustaining stably stratified runs, Cases SB, SC and SD, will also be presented. Cases SB and SC are identical to SA except they use smaller values for a_*/D, while SD is the same as SC save for a larger $Ri_{0,0}$. These simulations will be used to determine the effect of various initial stratification profiles upon the developed turbulent state.

For initial conditions, the runs use a neutral, fully developed $Re = 400$ velocity field from Case A90 of CFS*a* (i.e. NA90 of CFS*b*) with temperature profiles given by (7). No disturbances are added to the initial temperature field (the velocity fluctuations rapidly induce temperature fluctuations). We will show below that the resulting turbulence, after an initial transient, is in a state of local equilibrium with the mean field, and thus suffers no adverse effects from this initialization scheme.

A summary of the case parameters is given in table 1. Please note that the runs discussed in Chapter 5 of CFS*b*, which are defined by the same physical parameters and use the same notation (except SD) shown in table 1, yielded results that are slightly different than the results presented in this paper. The difference is due to a coding error, discovered after CFS*b* was published, that affected the process of stopping and restarting the run – a process necessary since the runs require more CPU time than is available during a single execution. Typically 5 or 6 such stops and restarts are needed. The error, which occurred during the retrieval of the velocity and temperature field coefficients at the beginning of an execution, was that about 3% of the temperature coefficients were incorrectly set to zero, and therefore caused minor differences between the previous and present results.

4.2. *Numerical parameters*

All computations were performed with the same number of grid points, N_x, N_y and N_z, horizontal domain size, L_x and L_y, and vertical lengthscale, Z (and consequently the same horizontal grid spacing Δx and Δy, and highest vertical quadrature point, z_{max}), that were used to resolve the unheated and heated $Re = 400$ flows presented in CFS*a* and CFS*b*. These values are given in table 2.

The stable temperature profile reduces the Case SA vorticity fluctuations, and thus the rate of kinetic energy dissipation, throughout the layer (see §5.1). So although the stratification will cause a decrease of some of the (largest) lengthscales (Métais & Herring 1989), the Kolmogorov scale is larger in stratified cases than in neutral ones; therefore the $(96 \times 96 \times 45)$ grid points, which proved adequate for the neutral flow, also adequately resolves the stratified turbulent velocity fields. The grid spacing is given by $\Delta x^+ = u_* \Delta x/\nu = u_* \Delta y/\nu \approx 7$, and 10 (unevenly spaced) vertical grid points within $z^+ = u_* z/\nu \approx 9$. Simulations that in the past have used this resolution have correctly reproduced both the turbulent physics and statistics of corresponding experimental data (Spalart 1988); we shall see below that this is in large measure also

Case	Re	Pr	$Ri_{0,0}$	a_*/D
SA	400	0.7	0.001	10
NSA	400	0.7	0.001	10
SB	400	0.7	0.001	5
SC	400	0.7	0.001	0.75
SD	400	0.7	0.002	0.75

TABLE 1. Physical parameters

N_x	N_y	N_z	L_x/D	L_y/D	Z/D	$z_{\max}/D$	$\Delta x/D$	$\Delta y/D$
96	96	45	26	26	3.3	24	0.3	0.3

TABLE 2. Numerical parameters

true here. Since all cases have $Pr = 0.7$, the grid spacing required for the velocity and temperature fields is similar, so the temperature variations should be accurately represented. (Because the pressure tends to 'smear' velocity fluctuations in a divergence-free flow, the resolution requirements are slightly more severe for the temperature field than for the velocity when $Pr = 1$. At $Pr = 0.7$, however, identical grid spacing for both fields has been found to be sufficient (Kim & Moin 1989; Rogers, Mansour & Reynolds 1989), and will be adopted here. Examination of the Case SA temperature spectra later proved this assumption valid.)

Since we are using DNS rather than LES, the change from neutral to stable stratification does not cause an increased modelling error. In DNS, as the stratification reduces the vertical size of the eddies, the smaller resolved scales contain more of the turbulent energy; in LES, less of the flow is resolved, making the computation more dependent upon the subgrid-scale model. Were we to use a numerical method that does not eliminate aliasing errors, the change could also diminish the accuracy of the DNS.

The maximum horizontal integral scale, over the height in the regions where the turbulence does not collapse, was found to be smaller than the corresponding scale in the unstratified flow. Therefore, the horizontal domain size $L_x \times L_y$ shown in table 2 is also satisfactory for the stable runs.

The NASA-Ames Advanced Computational Facility Cray-YMP was used to generate the simulations, which required about 9 CPU seconds per full timestep (three substeps). Case SA requires 6150 timesteps to advance from $tf = 0$ to $tf = 6.2$; the average step size was about $\Delta tf = 0.001$, $\Delta t^+ = u_*^2 \Delta t/\nu = 0.3$ or $G\Delta t/D = 0.2$.

5. Results: Cases SA and NSA ($a_* = 10D$)

We begin with Cases SA and NSA, for which $a_*/D = 10$ so that the lapse rate of the temperature profile (7) is finite in the entire turbulent region of the initial field. The parameters for these runs do not correspond precisely to any meteorological data set, but are similar enough to those found in the PBL that many of the physical properties – especially those insensitive to Reynolds number – of the simulated and actual PBL should correspond. In particular, the parameterizations that are valid for the PBL should also hold for the simulated layer, and the latter can therefore be used as a reliable data base for testing of the parameterizations.

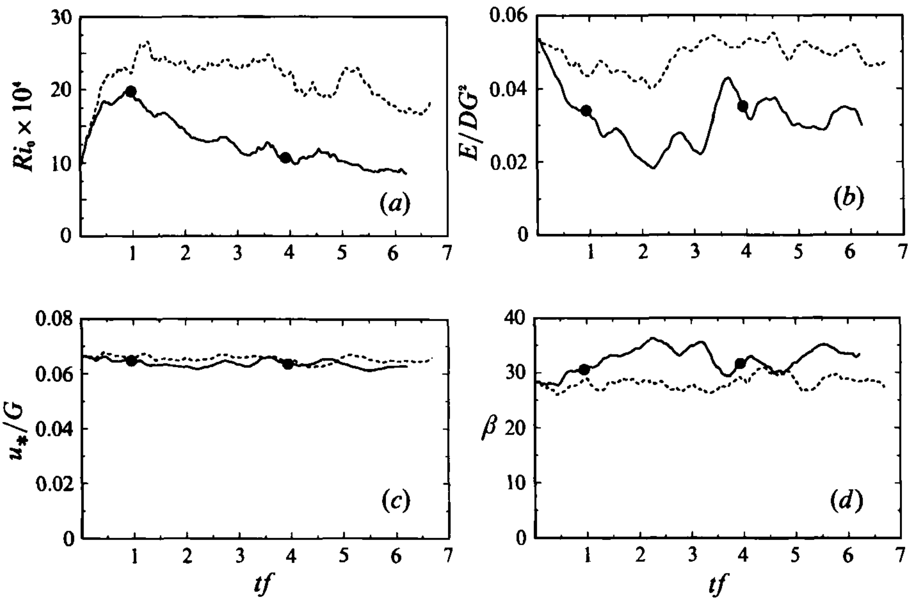

FIGURE 2. Time history of the (a) surface Richardson number, Ri_0, (b) volume integrated turbulent kinetic energy, E, (c) friction velocity at the surface, u_*, and (d) angle (deg.) between the geostrophic wind and surface shear stress, β: —, Case SA (stably stratified); ----, NSA (passive scalar). ●, Beginning and end of averaging period.

5.1. *Time histories*

In figure 2 time histories of the surface Richardson number, Ri_0 (or surface heat flux), the volume-integrated turbulent kinetic energy per unit area,

$$E = \frac{1}{2}\int_0^\infty q^2\,\mathrm{d}z$$

($q^2 = \langle u_i' u_i' \rangle$ is twice the turbulent kinetic energy averaged over a horizontal plane), the surface friction velocity, u_*, and the angle between the geostrophic wind and surface shear stress, β, are shown. Results from both the active (SA, solid curves) and passive (NSA, dashed) simulations are given. The initial adjustment period of both flows is about $tf = 0.5$, during which temperature fluctuations are generated by stirring of the 'painted on' temperature. Taking the height of the neutral layer to be 0.7δ (CFS*a*), where $\delta = u_*/f$ is the unstratified turbulent Ekman-layer lengthscale, we define an effective 'eddy turn-over' time, t_e, as the vertical average of q^2/ϵ (ϵ is the dissipation rate of $\frac{1}{2}q^2$). Initially, $t_e \approx 0.8/f$, so the initial adjustment period is about $0.6t_e$. After the initial adjustment, both the neutral and stable fields settle into slowly evolving states. For Case NSA, the fluctuations in figure 2(*b*–*d*) are purely statistical, whereas in figure 2(*a*) the variations represent both statistical and transient behaviour. All the figure 2 histories for Case SA contain statistical fluctuations with means that slowly drift in time. The long-term changes of the means are due to growth of the thermal boundary layer. Note that since the histories extend for a time of about an inertial time period ($2\pi/f$), the simulations have been run for on the order of a 'day'.

The differences between the active and passive scalar cases, which have identical initial temperature profiles (shown as the solid curve in figure 3*a*), can be attributed

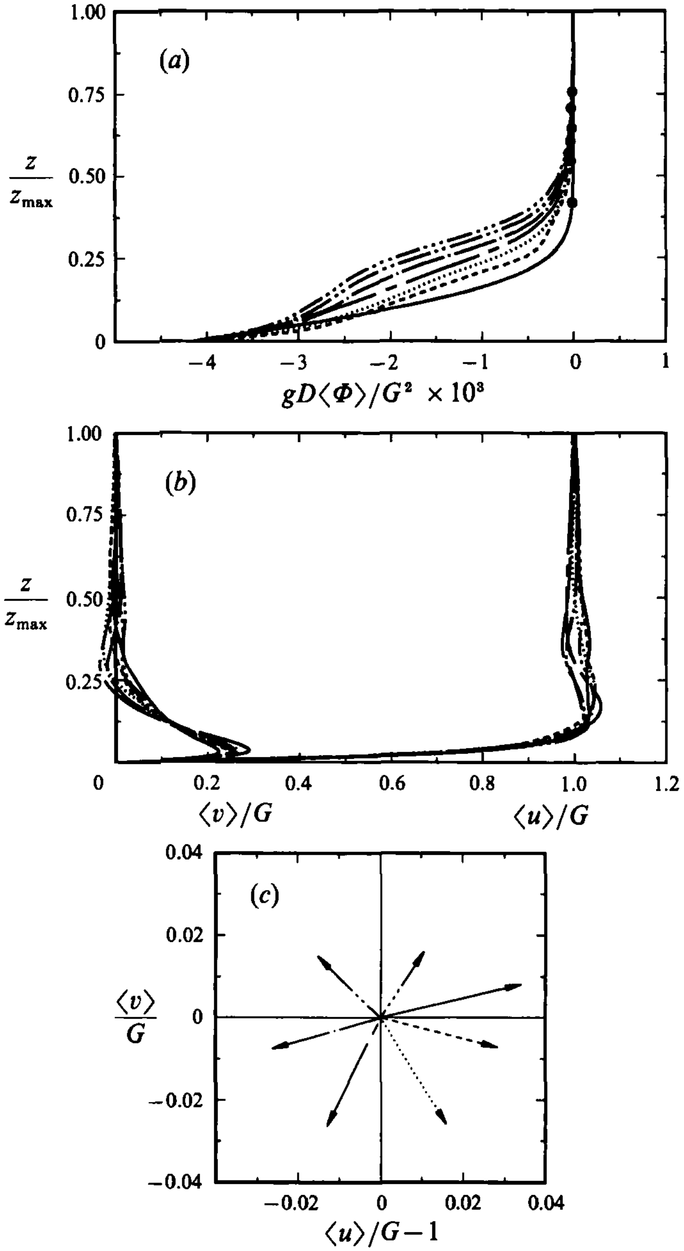

FIGURE 3. Mean temperature and velocity profiles for Case SA: —, $tf = 0$ (initial condition); ----, $tf = 0.95$; · · ·, $tf = 1.8$; ———, $tf = 2.9$; —·—, $tf = 3.9$; —··—, $tf = 5.0$; —···—, $tf = 6.2$. (*a*) Mean temperature (● marks elevation at which $\Gamma/\Gamma_0 = 0.01$), (*b*) mean velocity and (*c*) mean velocity defect at $z/z_{max} = 0.36$.

to the stabilizing effect of stratification. For example, the smaller heat flux (Ri_0) in Case SA is due to reduction of the turbulent mixing. As heavy, colder fluid is mixed upward (and warm lighter fluid, downward) part of the kinetic energy of the turbulence is lost to potential energy. The weakened turbulence, which (as we shall see below) contains both smaller vertical velocity and smaller vertical lengthscales

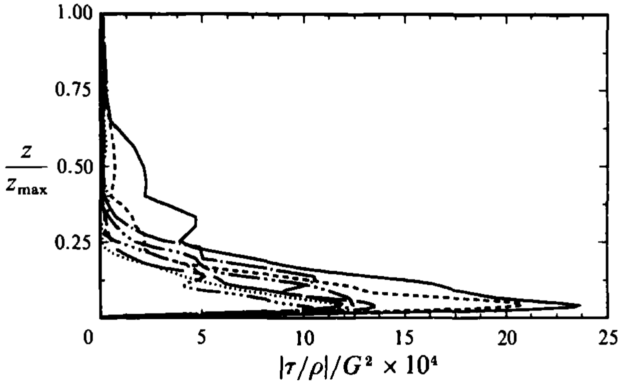

FIGURE 4. Reynolds shear stress magnitude, $|\tau/\rho| = (\langle u'w'\rangle^2 + \langle v'w'\rangle^2)^{\frac{1}{2}}$, for Case SA. Symbols as figure 3.

– and therefore a smaller effective turbulent diffusivity (proportional to the product of the two) – cannot transport warm fluid to the vicinity of the surface as effectively as the turbulence in a passive temperature field. The stable buoyancy reduces the heat flux by approximately one-third to one-half.

Despite the stabilizing influence of stratification, the turbulence in Case SA is still able to produce some mixing, as shown in figure 3(*a*) by the evolution of the mean temperature profile over the course of the simulation (unless stated otherwise, a 'mean' quantity is the result of an average over a horizontal plane). This plot also indicates that the surface gradient, Γ_0, first increases and then decreases with time, as shown in figure 2(*a*). The downward heat flux also gradually increases the fraction of the layer that is stratified. The initial temperature distribution is given by $a_*/D = 10$, so that $a_*/z_{max} = 0.4$, but for most of the run only the region above $z/z_{max} = 0.5$ is neutrally stratified. This is revealed by the upward migration of the solid symbols in figure 3(*a*), which denote the elevations at which the lapse rate is 1 % of Γ_0.

The stratification decreases the integrated turbulent kinetic energy by on average about 40% and increases the shear angle β by approximately 5°, compared to the neutral case (figures 2*b* and 2*d*). However, the shear angle remains significantly lower than the laminar 45° value because the layer remains turbulent. In fact, figure 2(*c*) shows that the magnitude of the surface stress is only slightly less than the unstratified value. This suggests that the buoyancy most strongly influences the outer part of the flow, leaving the energetic near-surface turbulence relatively unaffected – even though the lapse rate approaches zero as $z \to \infty$. The difference in β is due to the decreased depth of the turbulent region, and the increased turning of the velocity vector in the nearly laminar outer layer (more like that of the laminar Ekman flow). Further evidence for this will be provided below.

The effect of buoyancy on the mean velocity profile is presented in figure 3(*b*). One of the most noticeable influences is the formation of a local maximum in the velocity magnitude in the outer layer (most obvious near $z/z_{max} \approx 0.3$), indicating the presence of a weak 'nocturnal jet'. A nocturnal jet is often observed above the stable PBL (Wyngaard 1985), and can have a variety of causes, including the effects of terrain and the approach of a large-scale front (Stull 1988). Here, the jet is associated with the collapse of the turbulence in the outer part of the flow, as described by Blackadar (1957). Figure 4 shows that for $z/z_{max} \geqslant 0.3$, buoyancy significantly reduces the Reynolds shear stress. (Recall that the $tf = 0$ field is a realization of the

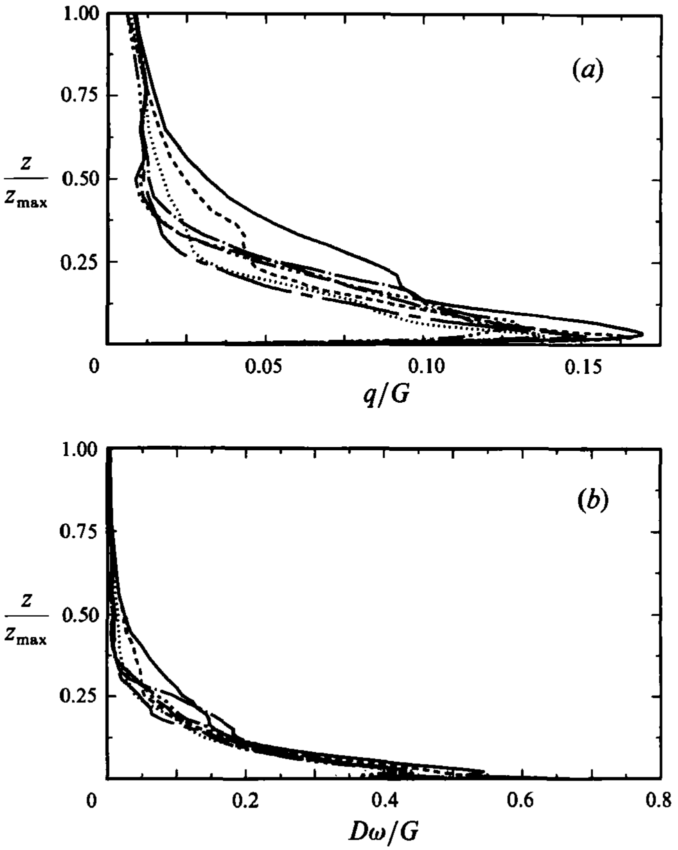

FIGURE 5. Profiles of r.m.s. fluctuations of (*a*) velocity, $q = (\langle u'u'\rangle + \langle v'v'\rangle + \langle w'w'\rangle)^{\frac{1}{2}}$, and (*b*) vorticity, $\omega = (\langle \omega_x'\omega_x'\rangle + \langle \omega_y'\omega_y'\rangle + \langle \omega_z'\omega_z'\rangle)^{\frac{1}{2}}$ for Case SA. Symbols as figure 3.

stationary, unstratified Case NSA flow. The (statistical) variation in time of the Case NSA Reynolds-stress profile is much less than the variation observed in figure 4.) This 'quenching' of the turbulent stress upsets a region that previously experienced a balance between the Reynolds stress divergence, Coriolis acceleration and horizontal pressure gradient. The remaining Coriolis and pressure-gradient terms result in an oscillation of the 'pre-quenched' velocity defect $\langle \boldsymbol{u}\rangle_{\mathrm{IC}} - \boldsymbol{G}$ about the unbalanced state at the inertial period $(2\pi/f)$ (Gill 1982) ($\langle \boldsymbol{u}\rangle_{\mathrm{IC}}$ is the mean velocity of the unstratified initial field). That is, the instantaneous mean velocity is the vector sum of $\boldsymbol{G}$ and the oscillating defect. This is illustrated in figure 3(*c*) which shows the behaviour of $\langle \boldsymbol{u}\rangle - \boldsymbol{G}$ at $z/z_{\max} = 0.36$. Because stratification does not exert a strong influence on the flow near the surface (as we shall soon see) where the velocity defect is largest, the jet in this simulation is much weaker than some observed in the atmosphere; wind speeds as large as twice G are common. (See for example, Thorpe & Guymer 1977 for analysis of the jet measured during the 1967 Wangara (Australia) field experiment. The direction of the inertial oscillation of the Wangara jet is opposite to that seen here because $f < 0$.)

Further effects of stratification are seen in the r.m.s. velocity and vorticity fluctuation profiles in figure 5. The curves represent the initial neutral state (the solid curves) and various states during Case SA. The buoyancy causes significant reductions of both q and ω in the outer layer. Above $z/z_{\max} \approx 0.3$, the vorticity

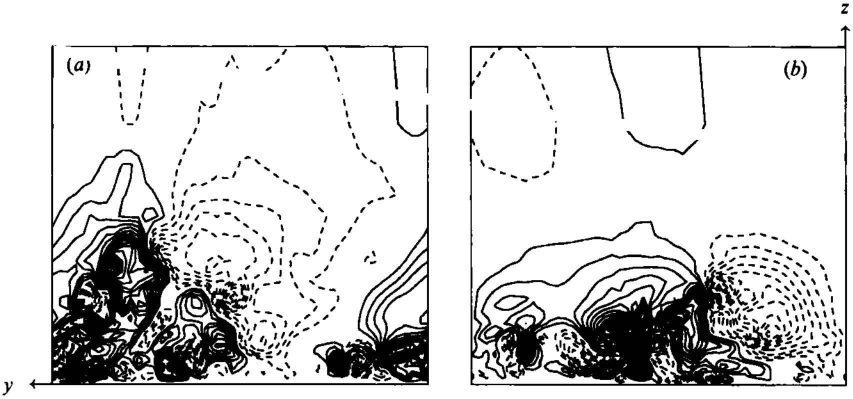

FIGURE 6. Contours of instantaneous vertical velocity on spanwise vertical (y,z)-planes for (a) Case NSA (passive scalar, at $tf = 0$) and (b) SA (stably stratified) at $tf = 3.9$: ——, $w/G > 0$; ----, $w/G < 0$; contour interval 0.008. Planes represent full flow domain.

fluctuations are practically zero, suggesting that the velocity fluctuations at $z/z_{\max} \geqslant 0.3$ are irrotational, and that in contrast to the neutral flow, the turbulent activity is confined to the lower third of the domain. The results presented in the next subsection show that this is indeed the case.

5.2. *Instantaneous fields*

Contours of instantaneous vertical velocity in a spanwise vertical plane in the neutral and stratified flows are shown in figure 6. The intensity and lengthscales of the turbulence near the surface are about the same as in the neutral layer, but the upper two-thirds of the stratified field is nearly laminar. Even though the lapse rate weakens with elevation (figure 3a), the outer regions of the flow are most strongly affected by the stratification. This is consistent with the observation that the larger spatial scales are more susceptible to buoyancy effects (Wyngaard 1982, p. 74). Therefore, there is only a range of intermediate elevations at which stratification is important, those where both Γ and the flow scale are large enough. In Case SA, all the turbulence is extinguished above $z/z_{\max} \approx 0.3$. The turbulence that existed in the neutral region $z \geqslant 0.5_{\max}$, where Γ is approximately zero, vanishes because the stratification closer to the surface cuts off the upward transport of kinetic energy that is the source of turbulence to the upper part of the layer under neutral conditions (see §5.3.2). (Conceivably, the 'unsustained' turbulence in the outer layer could temporarily transfer energy to the flow below.)

Stratification also influences the horizontal structure of the turbulence. In figure 7, contours of instantaneous streamwise velocity fluctuations in the horizontal planes at $z/z_{\max} = 0.11$, 0.28 and 0.45 are shown. The stratified turbulence is weaker at all three heights. The size of the horizontal eddies is also different. A measure of this difference is provided by the streamwise integral scale, given by

$$\int_0^{L_x} \langle u_i'(x,y,z)\, u_i'(x+r,y,z)\rangle \,\mathrm{d}r/q^2(z)$$

(sum on i). Where the turbulence is weak or non-existent, the lengthscale exhibits behaviour that is perhaps analogous to that observed experimentally during the stratification-induced collapse of turbulent wakes (Lin & Pao 1979) (in that both here

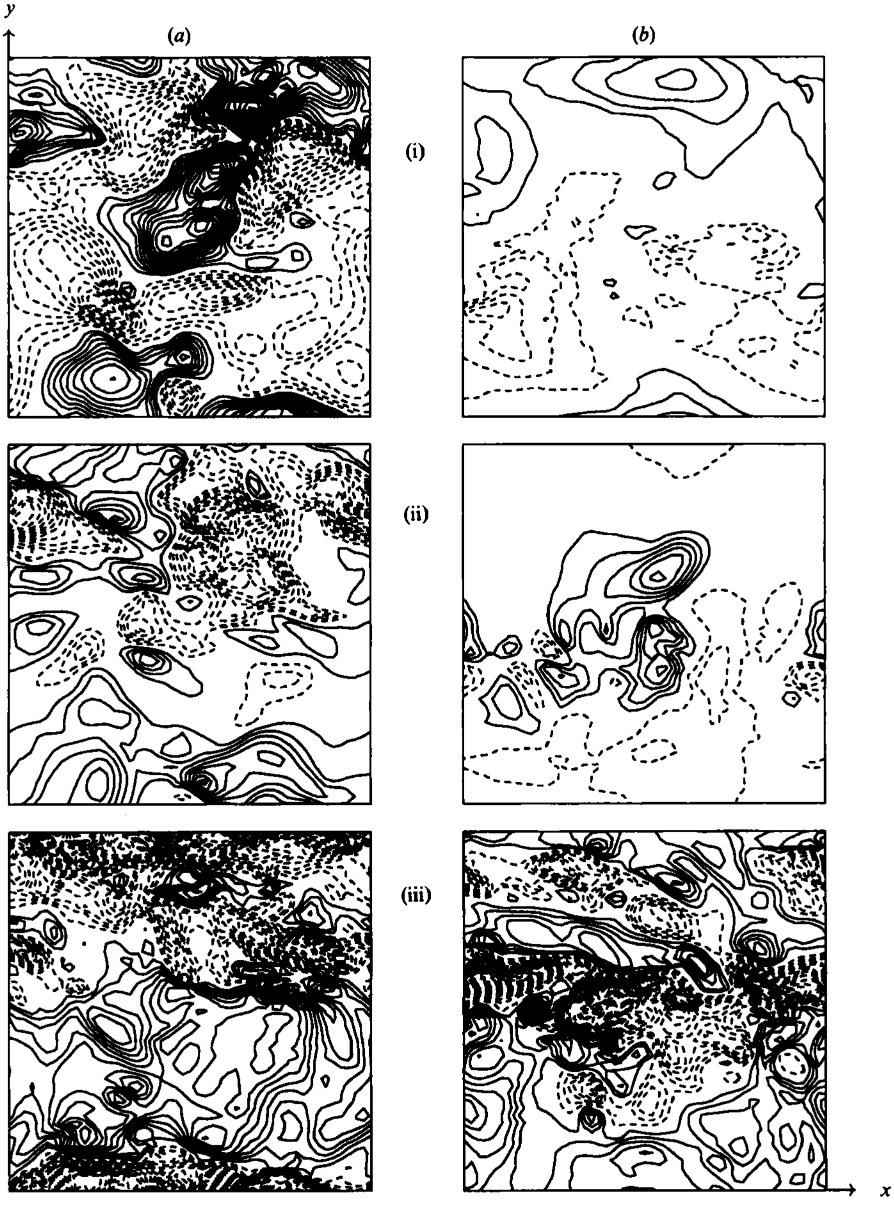

FIGURE 7. Contours of instantaneous streamwise velocity perturbation on horizontal (x, y)-planes for (*a*) Case NSA (passive scalar, at $tf = 0$) and (*b*) SA (stably stratified) at $tf = 3.9$. Free-stream flow from left to right. (i) $z/z_{\max} = 0.45$; (ii) $z/z_{\max} = 0.28$; (iii), $z/z_{\max} = 0.11$; —, $u'/G > 0$; ----, $u'.G' < 0$; contour interval is 0.015 for (ii) and (iii), 0.004 for (i). Planes represent full flow domain.

and for the wake, stratification leads to growth of the lengthscales in planes perpendicular to the gravity vector), since at $z/z_{\max} = 0.28$ and 0.45 the scale for the stratified flow is respectively 2.1 and 2.8 times the corresponding unstratified values at $tf = 0$. The opposite is true where the turbulence remains strong: at $z/z_{\max} = 0.11$ the stratified turbulence lengthscale is about 30% smaller than the neutral scale. Whether the buoyancy increases or diminishes the scale of the horizontal motions appears to be related to its ability to extinguish the turbulence. The fact that as long as the turbulence remains three-dimensional (that is, all three components of vorticity contain significant fluctuations) the vertical and horizontal scales remain coupled, due to 'continuity-driven' pressure interactions, would then explain the reduction in the streamwise scale at $z = 0.11z_{\max}$ in Case SA. In contrast, when the horizontal vorticity (ω_x' and ω_y') is small, as in runs where the turbulence dies (see CFS*b*), and in the later stages of Case SA for $z/z_{\max} \geqslant 0.30$, each fluid layer is free to move independently of the others. The increase in streamwise integral scale found in Case SA at $z/z_{\max} = 0.28$ and 0.45 could thus be the result of the collapsed turbulent flow transferring kinetic energy from small to large scales, which is typical of two-dimensional motions (such as those associated with vortex-merging in the mixing layer) (Kraichnan 1967). It could also be due simply to the more rapid destruction of small scales by viscosity, leaving only larger eddies, which decay at a slower rate, moving in horizontal planes in the post-turbulent flow.

5.3. *Time-averaged data*

A disadvantage of dealing with stratified turbulence is the unsteadiness of the mean flow, which prohibits averaging results of a single simulation over time (as was done for the statistically stationary neutral case presented in CFS*a*) to produce mean data profiles. Ensemble averages could be generated but the cost would be unreasonably high. Instead, we are, in general, forced to average only over horizontal planes. These average profiles are often quite rough, due to the finite sample size associated with a non-infinite horizontal domain, making differentiation of statistical fluctuations from physical effects difficult. (Examples of purely statistical fluctuations are given by the variations observed in figures 2*b*, 2*c* and 2*d* for Case NSA.) To avoid this difficulty, we note that the mean variation of the flow is slow, so short-term time averaging should give reasonable results. Unless otherwise stated, the remainder of the Case SA profiles discussed are the result of time averaging 120 fields, covering a time span of $\Delta tf = 3.0$, which corresponds to about four initial eddy turn-over times (as computed above). This time span was chosen because it represents a compromise between minimization of transient and statistical errors. The beginning and end of the sampling period are noted by the symbols in figure 2.

Changes in the (spatial) mean velocity profile that occur over the sampling period can be seen in figure 3(*b*). The dashed curve is the mean profile at the first time sample, the 'chain dot' curve, the last. The variations near $z = 0.3z_{\max}$ are evidence of the inertial oscillation of the nocturnal jet. Because the magnitude of the jet is relatively small, this phenomenon does not exert much influence on the time-averaged profiles.

The mean temperatures from the first and last time samples are shown in figure 3(*a*). Because it is affected only by gradients of the mean quantities, turbulence can be steady while the mean temperature varies with time, provided the lapse rate at each elevation does not change. In the present flow, however, the gradients vary with time because of the isothermal lower and zero-flux upper boundary conditions, but the variation is slow enough that quantities derived from the slope of the time-averaged $\langle \Phi \rangle$ profile (such as the gradient Richardson number defined below) should be meaningful.

The small difference between the Reynolds stress in the first ($tf = 0.95$) and last ($tf = 3.9$) samples, presented in figure 4, indicates that the turbulence adjusts quickly to changes in the mean profiles that occur during the averaging interval (the near-surface difference is thought to be mostly statistical; see figure 2*c*). In other words, the turbulence is in 'quasi-equilibrium'. Furthermore, because during the sampling

Case	u_*/G	β (deg.)	δ/D	L_*/δ	h/L_*	$h(\lvert f\rvert/u_* L_*)^{\frac{1}{2}}$
SA	0.0638	33.2	12.8	10.1	0.06	0.18
NSA	0.0654	28.0	13.1	∞	0	0
NA90	0.0652	28.5	13.0	—	—	—

TABLE 3. Time-averaged global results

period u_* oscillates about a value that is fairly constant (see figure 2*c*), these Reynolds stress profiles are evidence that it is reasonable to time average the Case SA data, especially for the hydrodynamic variables.

5.3.1. *Global quantities*

The global time-averaged momentum balance is much less precise than in the unstratified flow. In place of the 2% uncertainty found in the neutral-layer study (CFS*a*), the averaged stable field is out of equilibrium by about 17%. That is, when the steady-state terms in the mean (horizontal) momentum equation,

$$0 = 2\boldsymbol{\Omega} \times (\boldsymbol{G} - \langle \boldsymbol{u} \rangle) + \frac{\mathrm{d}}{\mathrm{d}z}\left(\frac{\boldsymbol{\tau}_{\mathrm{RS}}}{\rho_\infty} + \nu \frac{\mathrm{d}\langle \boldsymbol{u} \rangle}{\mathrm{d}z}\right)$$

(where $\langle \boldsymbol{u} \rangle = (\langle u \rangle, \langle v \rangle)$ and $\boldsymbol{\tau}_{\mathrm{RS}}/\rho_\infty = (-\langle u'w' \rangle, -\langle v'w' \rangle)$), is integrated over z, the difference between the ageostrophic and divergence terms in the direction perpendicular† to the surface shear stress is $0.17u_*^2$. The imbalance in the parallel directions is $0.09u_*^2$. These larger values are due to the smaller number of samples (almost six times as many samples were available in CFS*a*) and unsteadiness of the mean flow. Because a time average over the same number of fields of the (stationary) passive Case NSA data produces a velocity profile with an imbalance of 15 and 7% in the directions respectively perpendicular and parallel to the surface stress, the statistical error in the global momentum balance is probably at least as important as that due to drift in time of the mean. The global quantities derived from the time-averaged SA and NSA profiles are listed in table 3; for comparison the unstratified Case NA90 values computed in CFS*b* (same as A90 of CFS*a*) are given as well. Using the procedure discussed in CFS*a*, we estimate the uncertainty to be of the order of 1% for u_*/G and 3% for β in Case SA. As this is the same as in Case NA90, a significant fraction of the error in the surface stress can be attributed to the numerical sources of finite box size (which is also indirectly responsible for the statistical error) and finite space/time resolution.

The difference in β and the similarity of u_*/G for the neutral and stratified cases was discussed above. The ratio of the Oboukhov length, L_*, to the unstratified turbulent lengthscale, $\delta = u_*/f$, is $L_*/\delta = 10.1$ (where $L_* = -u_*^3 T_\infty/\kappa_{\mathrm{v}} g Q_0$, and κ_{v} is the von Kármán constant, taken to be 0.41). Since as $L_* \rightarrow 0$, the importance of stratification increases (Businger 1982), this value indicates that the stratification is relatively weak. Ratios as small as $L_*/\delta = 0.01$ have been observed in the nocturnal PBL (Nieuwstadt 1984). Although weak, this level of stratification is close to the maximum that can be imposed without totally quenching the turbulence at this

---

† In CFS*a* the component of the mean momentum equation *parallel* to the surface stress was used to measure the imbalance. The vector sum of both the 'shear-wise' and 'cross-shear' components of the imbalance is within 2% for all but two of the 15 turbulent runs presented in CFS*a*; for Cases A45W and A45S the vector measure is 2.8 and 3.6%, respectively.

Reynolds number (CFS*b*). Because the Reynolds number is low, the flow does not possess a pronounced logarithmic region (where $z/\delta \ll 1$ and $z/(\nu/u_*) \gg 1$), and is not close to the Reynolds-number-independent state that can accommodate both $L_*/\delta \ll 1$ and $L_*/(\nu/u_*) \gg 1$. A major difference therefore between the present and the more strongly stratified (higher *Re*) cases is the distance from the surface at which buoyancy becomes important. In Case SA only the outermost regions are directly affected by the stratification.

Also included in table 3 is the height of the stable layer, h, defined as the elevation at which the heat flux $\langle w'T'\rangle$ is 5% of the surface flux, Q_0 (see §5.3.3). For Case SA, $h = 0.30z_{\mathrm{max}}$, which corresponds to $h/L_* = 0.06$. The non-dimensional 'Zilitinkevich height', another stable-layer diagnostic,† is $h(|f|/u_* L_*)^{\frac{1}{2}} = 0.18$. Under strongly stable conditions, i.e. as $h/L_* \rightarrow \infty$, the Zilitinkevich parameter is close to 0.4 in the atmosphere (Garratt 1982). This is significantly larger than our result, but a number of theories predict a reduction in $h(|f|/u_* L_*)^{\frac{1}{2}}$ (irrespective of Reynolds number) to values comparable to that found here as the stability weakens (see figure 15*b* of Derbyshire 1990).

5.3.2. *Richardson numbers, length- and timescales*

One of the best indicators of the importance of stratification is the local Richardson number. Results from the time-averaged Case SA data set are shown in figure 8(*a*). Only the turbulent region, $z \leqslant h = 0.30z_{\mathrm{max}}$ is considered. Both the 'flux' and gradient' Richardson numbers, defined respectively as

$$Ri_{\mathrm{FL}} = \frac{g}{T_\infty} \frac{\langle w'T'\rangle}{\langle u'w'\rangle \mathrm{d}\langle u\rangle/\mathrm{d}z + \langle v'w'\rangle \mathrm{d}\langle v\rangle/\mathrm{d}z} \tag{8}$$

and

$$Ri_{\mathrm{GR}} = \frac{g}{T_\infty} \frac{\mathrm{d}\langle T\rangle/\mathrm{d}z}{(\mathrm{d}\langle u\rangle/\mathrm{d}z)^2 + (\mathrm{d}\langle v\rangle/\mathrm{d}z)^2}, \tag{9}$$

are presented. Physically, the Richardson numbers represent the relative importance of buoyancy and shear. Ri_{FL} is the ratio of the buoyant destruction (for stable flows) and the shear production terms in the turbulent kinetic energy equation. Note that the surface Richardson number is $Ri_0 = (Ri_{\mathrm{GR}})_0\ ((\mathrm{d}\langle u\rangle/\mathrm{d}z)_0^2 + (\mathrm{d}\langle v\rangle/\mathrm{d}z)_0^2) D^2/G^2$.

Figure 8(*a*) again shows that the importance of stratification increases with elevation. Although both the buoyant destruction and shear production fall to zero as $z \rightarrow \infty$, the latter approaches zero more rapidly. This demonstrates once more that the larger spatial scales are more sensitive to stable stratification. (Notice that because it is so weak, the shear associated with the nocturnal jet, discussed above, does not lead to a decrease in Richardson number in the outer layer.) There is strong evidence that the maximum gradient Richardson number at which turbulence can permanently exist in homogeneous flows at high Reynolds number is approximately 0.25 (Gerz *et al.* 1989; Holt *et al.* 1992; cf. Fleagle & Businger 1980, p. 282). Above

---

† The prediction that the equilibrium stable-layer height is proportional to $(u_* L_*/|f|)^{\frac{1}{2}}$ was originally derived by Zilitinkevich (1972) based on the assumptions that $h^2 \propto \nu_{\mathrm{T}}/f$ (by analogy to the laminar Ekman layer) and that ν_{T} scales with $u_* L_*$. The latter follows from the observation that in stably stratified turbulence the ratio of buoyant destruction to shear production of turbulent kinetic energy (the flux Richardson number) never exceeds a certain value. The height expression is also the result of similarity theories that assume the flow depends only on u_*, Q_0, g/T_∞, and f (Zilitinkevich 1975), and is a feature of Nieuwstadt's (1985) equilibrium model (see also Derbyshire 1990).

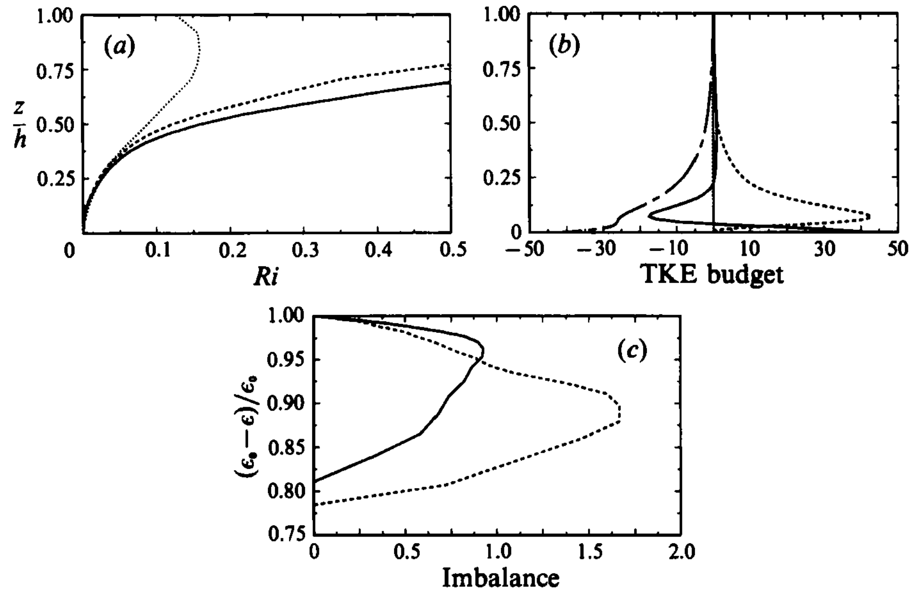

FIGURE 8. Turbulent kinetic energy budget profiles for Case SA (time averaged). (*a*) Richardson number: —, Ri_{FL}; ----, Ri_{GR}; ···, $Ri_* = -g\langle w'\Phi'\rangle/(-g\langle w'\Phi'\rangle+\epsilon)$. (*b*) Terms in steady-state budget, normalized by u_*^3/δ: ----, production, $-\langle u'w'\rangle \mathrm{d}\langle u\rangle/\mathrm{d}z-\langle v'w'\rangle \mathrm{d}\langle v\rangle/\mathrm{d}z$; ···, buoyant destruction, $g\langle w'\Phi'\rangle$; ———, viscous dissipation, $-\epsilon$; —, imbalance,

$$-[-\langle u'w'\rangle \mathrm{d}\langle u\rangle/\mathrm{d}z-\langle v'w'\rangle \mathrm{d}\langle v\rangle/\mathrm{d}z+g\langle w'\Phi'\rangle-\epsilon].$$

(*c*) Imbalances, $-[-\langle u'w'\rangle \mathrm{d}\langle u\rangle/\mathrm{d}z-\langle v'w'\rangle \mathrm{d}\langle v\rangle/\mathrm{d}z+g\langle w'\Phi'\rangle-\epsilon]$, normalized by u_*^3/δ: —, Case SA (time averaged); ----, Case NSA (passive scalar, averaged over SA sampling period).

$z = 0.6\,h$, where $Ri_{\mathrm{GR}} > 0.25$, the kinetic energy of the turbulence is supplied by transport from below. This is supported in figure 8(*a*) by the profile of Ri_*, defined as the ratio of buoyant to total (buoyant plus viscous) destruction: $Ri_* = -g\langle w'\Phi'\rangle/(-g\langle w'\Phi'\rangle+\epsilon)$. As can be seen from the steady-state turbulent kinetic energy transport equation,

$$0 = -\langle u'w'\rangle\frac{\mathrm{d}\langle u\rangle}{\mathrm{d}z}-\langle v'w'\rangle\frac{\mathrm{d}\langle v\rangle}{\mathrm{d}z}+g\langle w'\Phi'\rangle-\epsilon-\frac{\mathrm{d}J}{\mathrm{d}z},$$

if the divergence $-\mathrm{d}J/\mathrm{d}z$ of the kinetic energy flux,

$$J = \tfrac{1}{2}\langle u_i' u_i' w'\rangle-\tfrac{1}{2}\nu\, \mathrm{d}q^2/\mathrm{d}z-\nu d\langle w'w'\rangle/\mathrm{d}z+\langle p'w'\rangle/\rho_\infty,$$

were zero (and the flow is stationary), production would balance destruction and Ri_* would be identical to the flux Richardson number. The fact that Ri_* is less than Ri_{FL} implies the energy flux is a source of turbulent kinetic energy above $z = 0.25h$. Profiles of the production, buoyant destruction and viscous dissipation terms in the above balance are given in figure 8(*b*). Also shown, as the solid curve, is the imbalance in the steady-state budget, which represents an estimate of the flux divergence ($-\mathrm{d}J/\mathrm{d}z$ was not computed and recorded during the simulation). Mostly because of the time-discretization error discussed in §3, which causes $|\epsilon|$ to be a few percent too small, we expect $-\mathrm{d}J/\mathrm{d}z$ be somewhat larger than the imbalance, most noticeably in the outer layer (the tendency for $\partial\frac{1}{2}q^2/\partial t$ to be < 0 produces the opposite effect, to a lesser degree). For $z > \frac{1}{2}h$ the actual flux divergence is probably about 10 to 15% larger than the imbalance. To illustrate the effect of the stratification upon

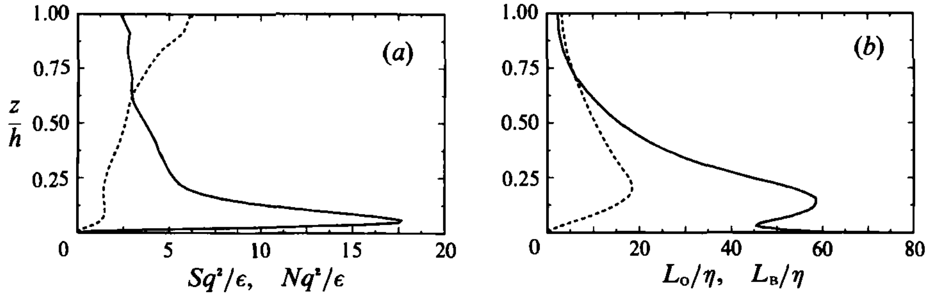

FIGURE 9. Profiles of (*a*) timescale and (*b*) lengthscale ratios for Case SA (time averaged): (*a*) —, Sq^2/ϵ; ----, Nq^2/ϵ. (*b*) —, L_O/η; ----, L_B/η.

the flux divergence, the outer-layer imbalance has been replotted in figure 8*c* against the 'dissipation defect', and compared to the imbalance found in the passive scalar flow. (The results were plotted versus ϵ since it is nearly monotonic, and accounts for the difference in depths of the two layers.) The profiles demonstrate that another important influence of the stratification is to significantly diminish the energy flux in the region between $z = 0.25h$ and h.

The turbulent Prandtl number, Pr_T, is $Ri_{GR}/Ri_{FL} = \nu_T/\kappa_T$. Figure 8(*a*) therefore implies that Pr_T is less than one for $0 \leqslant Ri_{GR} \leqslant 0.5$. Its behaviour will be investigated in §5.3.4.

In their recent LES study, Mason & Derbyshire (1990) computed fields with Richardson number profiles much different than those shown in figure 8(*a*). Their Richardson numbers do not increase monotonically with z, but reach a maximum of about 0.25 and fall to zero at higher elevations. Both their stratified flows and ours are produced by cooling an initially neutral field. The dissimilar behaviour is primarily due to the different ways in which the cooling is introduced, and the times at which the flows are examined. Whereas Case SA imposes a temperature with positive Γ extending to finite heights (i.e. $a_* > 0$), Mason & Derbyshire introduce buoyancy by reducing only the surface temperature ($a_* = 0$) and investigated the flow only during the period in which the outer regions remain unstratified and turbulent. If their simulation were continued, stable buoyancy would presumably diffuse upward so that, like Case SA, the higher elevations would become non-turbulent and Ri_{GR} would become very large – although because their *Re* is larger (and surface layer deeper), the time required for this to happen would be greater than in our low-*Re* flow. (In the PBL, an energetic nocturnal jet could also retard the $Ri_{GR} \rightarrow \infty$ process in the outer layer.) Mason & Derbyshire's simulation is representative of the early evening stable PBL, just after transition from convective to stable conditions, while Case SA is typical of the late night and early morning state. Despite the differences between the two studies, it is useful to compare some results, especially quantities that are believed to depend primarily on Richardson number; this is done in §5.3.5. DNS results from 'early evening', $a_* \approx 0$, cases will be presented in §6.

Another way to characterize the relative importance of competing mechanisms in turbulent flows is in terms of ratios of the length- or timescales associated with each mechanism. In figure 9(*a*) the vertical distributions of Sq^2/ϵ and Nq^2/ϵ are given. These can be interpreted as the ratios of the 'eddy turn-over' time (q^2/ϵ) to the timescales of the mean strain, $S^{-1} \equiv 2((\mathrm{d}\langle u\rangle/\mathrm{d}z)^2 + (\mathrm{d}\langle v\rangle/\mathrm{d}z)^2)^{-\frac{1}{2}}$, and buoyancy, $N^{-1} \equiv (g\Gamma/T_\infty)^{-\frac{1}{2}}$. N is the Brunt-Väisälä or 'buoyant' frequency (the frequency at which a slightly displaced particle in a quiescent inviscid fluid with lapse rate Γ oscillates about its equilibrium position (Turner 1973)). The ratio of the two timescales is $N/S = (2Ri_{\mathrm{GR}})^{\frac{1}{2}}$. The Sq^2/ϵ profile (the solid curve in figure 9*a*) is similar to those found in two-dimensional turbulent boundary layers; it exhibits a near-surface maximum of between 15 and 20 and falls to about 2.5 in the outer layer (see results of Kim, Moin & Moser 1987 presented in Lee, Kim & Moin 1990). This distribution shows that near the surface, mean shear is more important than the 'self-interaction' of the turbulence, but not so large that nonlinear interactions are negligible; in other words, rapid distortion theory (Townsend 1976) is not directly applicable. Far from the surface, where Sq^2/ϵ is $O(1)$, the 'external' and 'self-induced' strains are comparable.† The behaviour of Nq^2/ϵ suggests that the importance of buoyancy relative to self-straining increases with elevation.

Lengthscale data for Case SA are shown in figure 9(*b*). The ratios of the Ozmidov and the buoyancy lengthscales to the Kolmogorov scale are given. The Ozmidov scale, $L_{\mathrm{O}} \equiv (\epsilon/N^3)^{\frac{1}{2}}$, represents the vertical scale at which buoyancy and inertial forces are equal. It is therefore the largest vertical scale of motion that can exist in a stratified flow (Ozmidov 1965; Turner 1973). The buoyancy scale, L_{B}, is defined as σ_w/N (σ_w is the square root of the variance of the vertical velocity), and also represents a buoyancy-limited maximum scale. L_{B} is the vertical distance over which significant kinetic-to-potential energy conversion occurs (Wyngaard 1985). Since the physical concepts behind the two scales are equivalent, differences that occur in practice (apart from a constant of order one) are the result of using an incomplete model to represent the turbulence (for example, anisotropy is neglected in the definition of L_{O}).

Because the Kolmogorov scale, $\eta = (\nu^3/\epsilon)^{\frac{1}{4}}$, is the smallest (dissipation) scale of the turbulence, L_{O}/η and L_{B}/η define the 'bandwidth' available to the turbulence at each elevation (Gregg 1987). The ratio $(L_{\mathrm{O}}/\eta)^{\frac{4}{3}} = \epsilon/N^2\nu$ can be interpreted as a local turbulent Reynolds number, Re_{T} – if the velocity scale is σ_w, the lengthscale l is L_{B} and $\epsilon = \sigma_w^3/l$ (these last two expressions will be discussed below; see (10)–(13)). Therefore, $L_{\mathrm{O}}/\eta = Re_{\mathrm{T}}^{\frac{3}{4}}$. Figure 9(*b*) implies that the range of scales available to the flow between $z/h \equiv 0.6$ and 1 is quite small. As we examine this flow, we must bear in mind that only the 'core' of the layer, $0.05 \leqslant z/h \leqslant 0.6$, is strongly turbulent.

Another consequence of the reduction with elevation of the range of lengthscales is that internal waves‡ are not apt to be present in the outer layer; since L_{B}, L_{O} and η are of the same order, any waves that might appear are likely to be quickly damped by viscosity. Stillinger, Helland & Van Atta (1983) observed that internal waves disappeared, in their stratified grid turbulence experiments, when L_{O}/η fell below about 10, the value near $z = 0.6h$ in Case SA. In the strongly turbulent regions of this flow (where the lengthscale ratios are larger) waves are also probably absent (or at least not significant), since the statistics for stratified and unstratified turbulence are very similar. The importance of buoyancy waves in non-turbulent regions is discussed in CFS*b*.

---

† For high Reynolds number flows, the timescales of the largest and smallest eddies will be very different, i.e. $\omega q^2/\epsilon \gg 1$. Therefore, at high Re nonlinear interactions can also be important where Sq^2/ϵ is large, since S/ω will not necessarily also be large.

‡ Here we consider only waves generated by turbulence; buoyancy waves that result from large-scale topographic features (e.g. mountains) or synoptic-scale disturbances will not appear because of the assumed flow conditions.

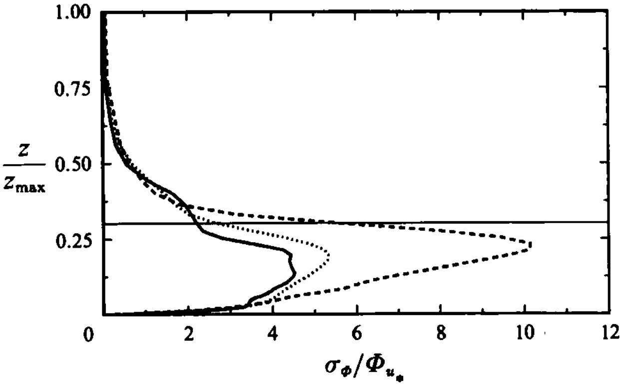

FIGURE 10. Profiles of r.m.s. temperature fluctuations for Case SA: —, $tf = 0.95$; ----, $tf = 3.9$; · · ·, time averaged. Horizontal line denotes $z = h$. $\Phi_* = |Q_0|/T_\infty u_*$.

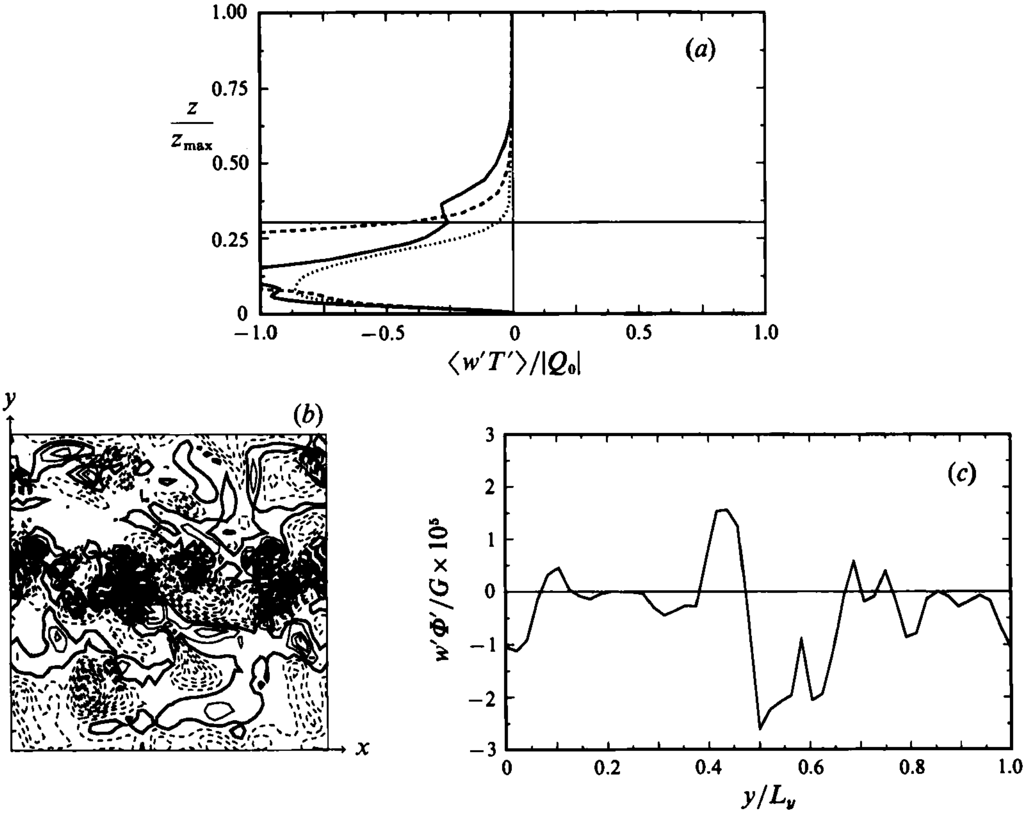

FIGURE 11. Turbulent heat flux for Case SA. (a) —, $tf = 0.95$; ----, $tf = 3.9$; · · ·, time averaged. Horizontal line denotes $z = h$. (b) Instantaneous flux on horizontal (x, y)-plane at $z/z_{\max} = 0.11$ at $tf = 3.9$. Free stream flow from left to right: —, $w'\Phi'/G > 0$; —, $w'\Phi'/G = 0$; ----, $w'\Phi'/G < 0$. Maximum is 1.0×10^{-4}; minimum, -1.7×10^{-4}. Contour interval 0.5×10^{-5}. (c) Spanwise variation of instantaneous flux at $x/L_x = 0.5$ of horizontal plane shown in (b).

5.3.3. *Temperature fluctuations, heat flux*

We now turn our attention to the behaviour of the temperature fluctuations and heat flux, shown in figures 10 and 11, respectively. The solid and dashed curves in figures 10 and 11(a) denote respectively the first and last samples from which the

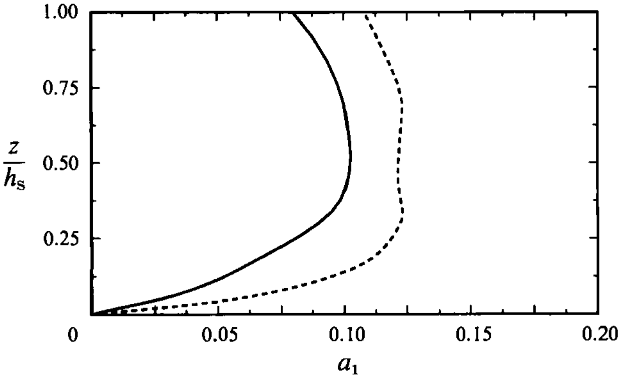

FIGURE 12. Ratio of Reynolds shear stress magnitude to twice turbulent kinetic energy, $a_1 = (\langle u'w'\rangle^2 + \langle v'w'\rangle^2)^{\frac{1}{2}}/q^2$: —, Case SA (time averaged); ----, NSA (passive scalar, averaged over SA sampling period).

time-averaged profile is constructed; the average is given by the dotted curves. The horizontal lines mark the height of the layer, h (defined via the 5% heat flux criterion, for the time-averaged data). A change of σ_Φ in time is apparent (σ_Φ is normalized by $\Phi_* = |Q_0|/T_\infty u_*$, where Q_0 and u_* are derived from either the local (for the $tf = 0.95$ and 3.9 curves) or time-averaged temperature and velocity profiles). On the other hand, much of the change in $\langle w'\Phi'\rangle/|Q_0|$ is probably statistical, since the instantaneous curves both fall mostly to the same side of the time-averaged result. (The instantaneous profiles in figure 11*a* are normalized by the instantaneous surface flux, $Q_0(t) \propto \Gamma_0(t)$, while the time-averaged distribution is divided by Q_0 given by Γ_0 for the time-averaged temperature.) The rates at which σ_Φ and $\langle w'\Phi'\rangle$ fall to zero at large z are quite different. While the time-averaged heat flux becomes zero at about the same elevation as the vorticity (figure 5*b*) and Reynolds shear stress (figure 4), the decay of the temperature disturbances resembles that of the velocity fluctuations (see figure 5*a*). At first glance, it might appear that these velocity and temperature perturbations are associated with internal waves. However, since $\Gamma \approx 0$ here, and figure 5(*a*) reveals that the velocity fluctuations at each elevation never exceed those found in the neutral initial condition, it is more likely that the non-zero σ_Φ is due to fluctuations of an effectively passive scalar, which has diffused from below.

Contours of the instantaneous heat flux, $w'\Phi'$, in the horizontal plane at $z/z_{\max} = 0.11$ are shown in figure 11(*b*). While the positive and negative values occupy about the same area, the negative peaks are stronger. An example of this is provided in figure 11(*c*) by the variation of $w'\Phi'$ with y along a line of constant x. The average, $\langle w'\Phi'\rangle$, is negative (as shown by figure 11*a*), indicating that on the average the turbulence is working against the stratification, converting kinetic energy into potential energy (i.e. σ_Φ). The mean potential energy is thereby increased.

5.3.4. *Hydrodynamic quantities, turbulent Prandtl number*

When normalized by the surface friction velocity, both the normal and shear components of the time-averaged Reynolds stresses (not shown) are only slightly smaller near the surface than their unstratified counterparts (cf. CFS*b*). Coupled with the minor difference in u_* for the active and passive cases shown in figure 2(*c*), this reinforces the notion that the near-surface regions of the two flows are similar.

Figure 12 gives the Reynolds stress ratio, $a_1 = (\langle u'w'\rangle^2 + \langle v'w'\rangle^2)^{\frac{1}{2}}/q^2$. So that we may compare stratified and neutral results, the vertical axis in figure 12 (and the two to follow) have been normalized by the 'stress height', h_S, the elevation at which the

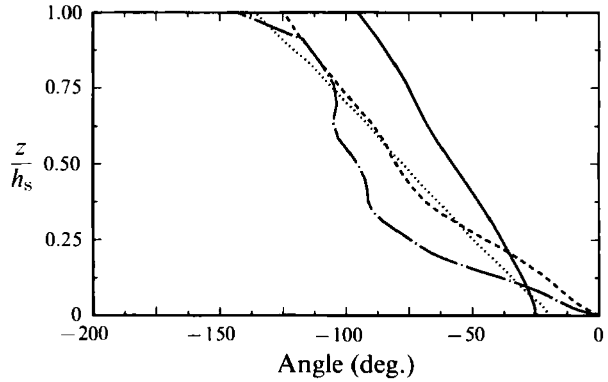

FIGURE 13. Direction of Reynolds shear stress $(-\langle u'w'\rangle, -\langle v'w'\rangle)$ and velocity gradient $(\mathrm{d}\langle u\rangle/\mathrm{d}z, \mathrm{d}\langle v\rangle/\mathrm{d}z)$ vectors, measured from orientation of surface shear stress. Case SA (time averaged): —, Reynolds stress; ----, velocity gradient. Case NSA (passive scalar, averaged over SA sampling period): ····, Reynolds stress; —·—, velocity gradient.

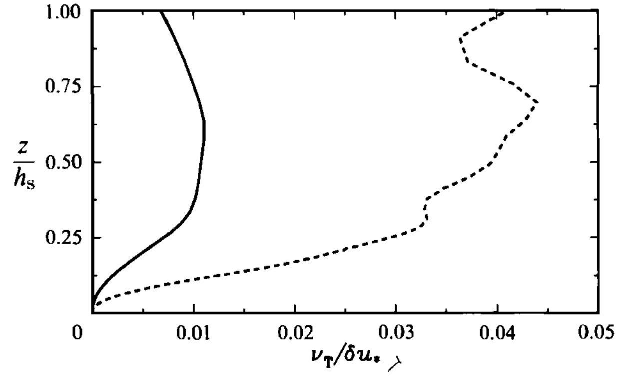

FIGURE 14. Eddy viscosity, $\nu_T = P_S/(2S)^2$: —, Case SA (time averaged); ----, NSA (passive scalar, averaged over SA sampling period).

Reynolds shear stress magnitude $(\langle u'w'\rangle^2 + \langle v'w'\rangle^2)^{\frac{1}{2}}$ is 5% of the surface stress. (A heat flux height may be computed for Case NSA, but because the temperature does not affect the turbulence for a passive scalar flow, h_S is a better measure of the turbulent depth.) For Case SA, $h/h_S = 1.69$, and the stress height is 0.49 times the Case NSA value of h_S. In the stratified layer a_1 is smaller than in the neutral layer, a result of the buoyancy diminishing the vertical velocity. (The fact that the unstratified value is also less than the usual $a_1 \approx 0.16$ found in two-dimensional boundary layers is a consequence of the system rotation; cf. figure 16 of CFS*a*.) The Reynolds shear stress is reduced more than the turbulent kinetic energy, of which σ_w^2 is only one component.

A comparison of the directions of the projected Reynolds shear stress and velocity gradient is provided in figure 13. In the neutral layer both the stress and gradient turn through wider angles than in the stable layer. We also note that the oft-made assumption that the Reynolds stress is aligned with the velocity gradient is of comparable, but not high, accuracy in both flows. The angle between the two is as large as 25°.

One of the most striking differences between the stable and neutral flows is in the behaviour of the eddy viscosity, ν_T. As shown in figure 14, ν_T is as much as three and a half times larger in the unstratified case. (The normalization does not cause the

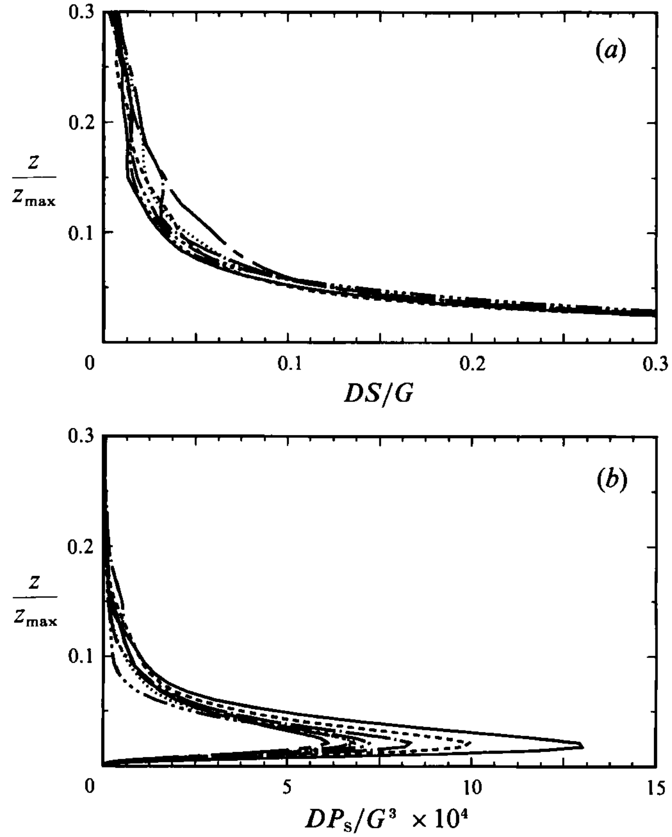

FIGURE 15. Profiles of (*a*) mean velocity gradient magnitude and (*b*) rate of production by shear of turbulent kinetic energy for Case SA.

$S = \frac{1}{2}[(\mathrm{d}\langle u\rangle/\mathrm{d}z)^2+(\mathrm{d}\langle v\rangle/\mathrm{d}z)^2]^{\frac{1}{2}}$; $P_{\mathrm{S}} = -\langle u'w'\rangle\,\mathrm{d}\langle u\rangle/\mathrm{d}z-\langle v'w'\rangle\,\mathrm{d}\langle v\rangle/\mathrm{d}z$.

—, $tf = 0$ (initial condition); ----, $tf = 0.95$; · · ·, $tf = 1.8$; ——, $tf = 2.9$; —·—, $tf = 3.9$; —· ·—, $tf = 5.0$; —· · ·—, $tf = 6.2$.

difference, since u_* and δ are very similar for the two flows; see table 3.) The definition of the eddy viscosity used here is $\nu_{\mathrm{T}} = P_S/(2S)^2$, where

$$P_S = -\langle u'w'\rangle\,\mathrm{d}\langle u\rangle/\mathrm{d}z-\langle v'w'\rangle\,\mathrm{d}\langle v\rangle/\mathrm{d}z$$

is the production rate due to shear of the turbulent kinetic energy, and $2S = ((\mathrm{d}\langle u\rangle/\mathrm{d}z)^2+\mathrm{d}\langle v\rangle/\mathrm{d}z)^2)^{\frac{1}{2}}$ is the magnitude of the mean velocity gradient. When the eddy viscosity is defined as $\tilde{\nu}_{\mathrm{T}} = ((\langle u'w'\rangle^2)+(\langle v'w'\rangle)^2)^{\frac{1}{2}}/2S$, the Case NSA-to-Case SA ratio is still about 3.5 to 1. (As shown in CFS*a*, $\tilde{\nu}_{\mathrm{T}}$ is slightly larger than ν_{T}.) Since $\tilde{\nu}_{\mathrm{T}}$ decreases more than the Reynolds shear stress (figure 4), the stable flow also has a larger mean velocity gradient. The increase can be observed in figure 15(*a*). Near $z = 0$ (not shown in figure 15*a*), the u_* history (figure 2*c*) implies that the gradient decreases slightly (cf. table 3; recall $S_0 \sim u_*^2$). Nevertheless, in most of the layer the buoyancy leads to a larger S. This increase in velocity gradient does not, however, lead to a significant increase in P_S. In fact, figure 15(*b*) shows that near the surface the production rate is actually diminished.

The stratification also noticeably affects the turbulent transport of heat. This is

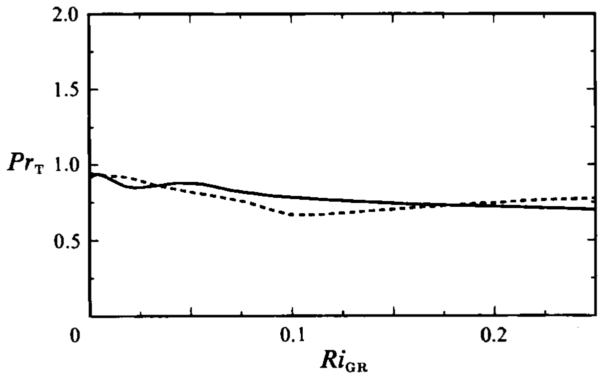

FIGURE 16. Variation of turbulent Prandtl number, $Pr_T = Ri_{GR}/Ri_{FL} = \nu_T/(-\langle w'\Phi'\rangle/\mathrm{d}\langle\Phi\rangle/\mathrm{d}z)$, $\nu_T = P_S/(2S)^2$: —, Case SA (time averaged); ----, NSA (passive scalar, averaged over SA sampling period).

indirectly revealed by the variation with Ri_{GR} of the turbulent Prandtl number shown in figure 16. (Recall that Ri_{GR} ranges from 0 at the surface to 0.25 at about $z = 0.6h$.) The similarity between the behaviour in the stable and neutral cases implies that as the buoyancy lessens ν_T (figure 14), it also reduces the turbulent conductivity by about the same amount. Figure 16 also shows – since $Pr_T \equiv Ri_{GR}/Ri_{FL}$ – that the stratification diminishes the flux $\langle w'\Phi'\rangle$ about as much as it does P_S (cf. Gerz *et al.* 1989). For both flows, Pr_T falls between 0.5 and 1, the range found in experimental observations of (unstratified) two-dimensional boundary layers (Kays & Crawford 1980).

5.3.5. *Reynolds-averaged closures*

In this section we shall use the Case SA data to test some Reynolds-averaged closure models. One of the most popular schemes for stably stratified layers is the second-order parameterization of Brost & Wyngaard (1978) (see Fitzjarrald 1979 for a more complete presentation of the details of the model). Their principal assumptions include the neglect of time variation and third-order moments in the transport equations for the second-order correlations, and a limit on the largest spatial scale caused by buoyancy. Away from the surface, the lengthscale is assumed proportional to $L_B = \sigma_w/N$. This is often referred to as the constant-Froude-number approximation (Wyngaard 1985).

Nieuwstadt (1984) used the Brost–Wyngaard approach as the basis for a similarity theory (see also Sorbjan 1986). The cornerstone of the scheme (and Brost & Wyngaard's model) is the idea that in stably stratified flows, the state of the turbulence depends only upon local conditions at a given elevation. When non-dimensionalized by the local friction velocity, $u_\times(z) \equiv (\tau/\rho)^{\frac{1}{2}}$, and local Oboukhov length, $\Lambda(z) \equiv -u_\times^3 T_\infty/\kappa_v g\langle w'T'\rangle$ (we assume $\kappa_v = 0.41$), the model equations contain only a single parameter and are universal in this sense. (Note that as $z \to 0$, $u_\times \to u_*$ and $\Lambda \to L_*$.) The 'similarity' lies in the equations governing the turbulence profiles, not the profiles themselves, as is usually the case. Nieuwstadt chose as the independent parameter the normalized near-surface 'large eddy' lengthscale z/Λ. Turbulence statistics are assumed to exhibit a unique dependence upon this parameter. Because the large-eddy scale is assumed to become independent of z far from the surface, locally normalized statistics should become constant at large z/Λ. This regime is referred to as 'z-less' stratification (Wyngaard 1973).

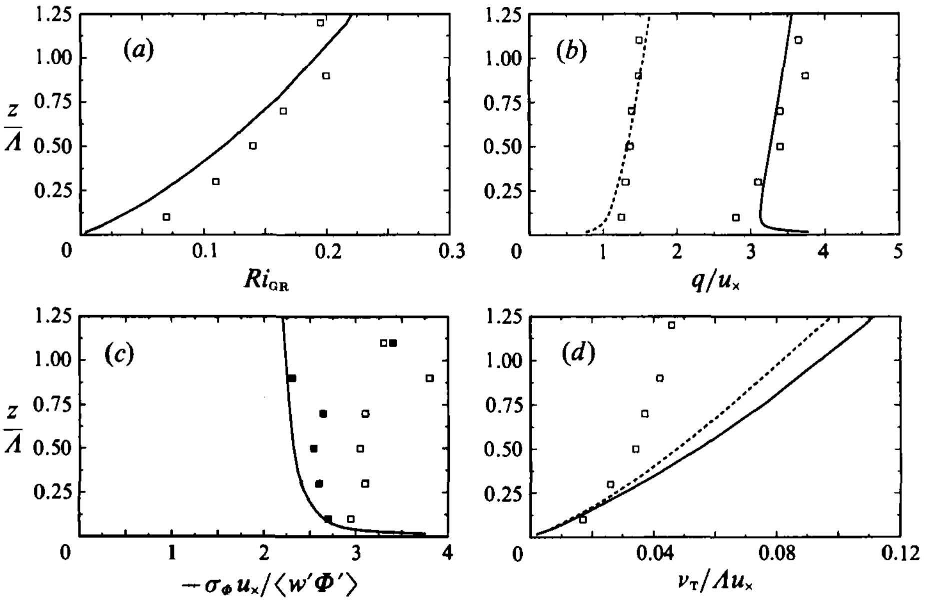

FIGURE 17. Local scaling for Case SA (time averaged): □, Nieuwstadt's (1984) unfiltered atmospheric data; ■, filtered† atmospheric data. (*a*) Gradient Richardson number; (*b*) r.m.s. velocity fluctuations: —, total velocity; ----, vertical; (*c*) r.m.s. temperature fluctuations; (*d*) eddy viscosity, —, $\tilde{\nu}_T = |\tau/\rho|/2S$; ---, $\nu_T = P_S/(2S)^2$.

Some of the time-averaged Case SA data are plotted using the local scaling in figure 17. Also included in these figures are Nieuwstadt's (1984) atmospheric measurements, gathered from a 200 m tower in the Netherlands. This is a rather rigorous test of the local scaling concept given the mild stratification and low Reynolds number of the DNS. Nevertheless, the agreement between the Richardson numbers and r.m.s. velocity fluctuation profiles of the two data sets, shown in figures 17 (*a*) and 17 (*b*), is surprisingly good. Only data from the regions in which the flow is strongly turbulent (i.e. where the turbulent Reynolds number is large, see figure 9*b*) are used, to avoid low-Reynolds-number effects. The maximum z/Λ considered, 1.25, corresponds to $z/h = 0.6$. Because Ri_{GR} is not constant, the flow in this range is not 'z-less'; that is, it is influenced by the surface. If the stratification were increased (provided the turbulence did not collapse), z/Λ would increase at a given elevation, and the effect of the surface would diminish. The local scaling theory predicts that the Richardson number would then become independent of height. (When the large-eddy scale does not depend on z, the modelled turbulent kinetic energy equation requires that the Richardson number be constant with elevation (Nieuwstadt 1985).) The strongly stable atmosphere often exhibits this feature, with $Ri_{GR} \approx 0.2$ over considerable heights (Mahrt *et al.* 1979; Nieuwstadt 1984, 1985). Constant values of Ri_{GR} near 0.1 have also been found (Garratt 1982).

The agreement between the locally scaled atmospheric and DNS temperature fluctuations and eddy diffusivities, figures 17(*c*) and 17(*d*), is poorer. The DNS temperature fluctuations do, however, fall fairly close to the atmospheric data that were filtered to remove low-frequency oscillations thought to be associated with gravity waves (the solid symbols), and the model profile for ν_T predicted by

---

† For (*a*), (*b*) and (*d*) the filtered data are either not available or not appreciably different from the unfiltered values; see Nieuwstadt (1984).

Nieuwstadt's normalized transport equations lies about as close to the DNS curves as it does to the lower values (cf. figure 4 of Nieuwstadt 1984). Despite the discrepancies in the σ_Φ and ν_T results, the agreement of the Richardson number and r.m.s. velocity fluctuations, especially in the light of the low Reynolds number and mild stratification of the simulation, tends to support the validity of the local scaling.

The DNS results can also be used to provide more direct tests of closure schemes, as we will now demonstrate. Two approaches are commonly used to parameterize the lengthscale that sets the dissipation rate in stratified flows. The first is due to Brost & Wyngaard (1978). It approximates the dissipation length

$$L_\epsilon \equiv C_\epsilon q^3/\epsilon \tag{10}$$

in stratified wall-bounded flows by

$$L_\epsilon^{-1} \approx L_{\mathrm{BW}}^{-1} = \frac{1}{z} + \frac{N}{A_N \sigma_w} \tag{11}$$

with $A_N = 1.69$ and $C_\epsilon = 0.139$. As noted previously, this is based on the hypothesis that the largest vertical scale of the turbulent motions in stratified flows is determined by the smaller of the distance from the surface and the buoyancy scale, $L_{\mathrm{B}} = \sigma_w/N$.

Alternatively, Hunt, Stretch & Britter (1988) (see also Hunt, Spalart & Mansour 1987) proposed as a model of another 'critical eddy scale',

$$l_\epsilon \equiv \sigma_w^3/\epsilon, \tag{12}$$

the expression

$$l_\epsilon^{-1} \approx l_{\mathrm{HSB}}^{-1} = \frac{A_{\mathrm{B}}}{z} + \frac{2A_S S}{\sigma_w}, \tag{13}$$

where $2S$ is the magnitude of the mean shear, $((\mathrm{d}\langle u\rangle/\mathrm{d}z)^2 + (\mathrm{d}\langle v\rangle/\mathrm{d}z)^2)^{\frac{1}{2}}$. As in the Brost–Wyngaard model, a harmonic mean is employed to emphasize the smaller of the inner ('blocking') and outer ('shear') scales. The reason for neglecting the direct influence of stratification and recommending (13) is the assumption that the dissipation rate is set by the mean strain rate, not the stratification. This is consistent with the fact that the shearing scale, $\sigma_w/2S$, is typically smaller than the buoyancy scale in stratified turbulence (Hunt *et al.* 1985, 1988). The 'blocking' model constant A_{B} has been chosen to be 0.27 by examining shear-free boundary layers and the 'shearing' constant A_S is found to be 0.45 by matching the logarithmic boundary-layer region.

The two models are compared in figure 18(*a*). Both the Brost (dashed curve) and Hunt (dotted) models are normalized by the actual lengthscales, $C_\epsilon q^3/\epsilon$ and σ_w^3/ϵ, respectively. Perfect agreement between data and parameterization would result in a constant value of one. Also shown are the model predictions with the z^{-1} terms left out, to illustrate the importance of the blocking contributions. The difference between the 'blocked' and 'unblocked' predictions is much smaller for the Hunt model than for Brost's, to which the z^{-1} term contributes significantly throughout the layer. Away from the surface ($z/h > 0.25$), l_{HSB} is too large by as much as 70%, whereas L_{BW} is also too large, but by no more than about 30%. The over-prediction of the models may be partially attributed to the low Reynolds number of the simulation. (Note that any variation associated with the uncertainty in ϵ in the outer layer due to the time-discretization error discussed in §3 would cause an underprediction of the model-to-DNS ratios, and would be of much smaller

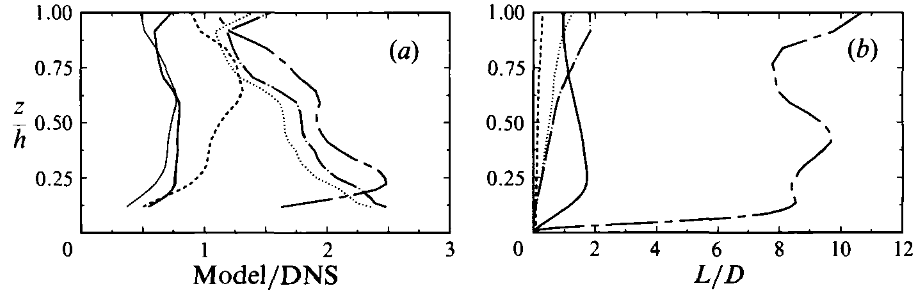

FIGURE 18. Lengthscale profiles for Case SA (time averaged). (*a*) Ratio of predicted to observed value: ----, Brost & Wyngaard (1978), Eqn. (11); · · ·, Hunt *et al.* (1988), Eqn. (13); ———, Brost & Wyngaard without blocking term; —·—, Hunt *et al.* without blocking; —, Brost & Wyngaard with Perry *et al.*'s (1985) Reynolds number correction (using $C_1' = 2.8$); —, Hunt *et al.* with Reynolds number correction. (*b*) —, σ_w/N; ———, q^3/ϵ; · · ·, $\sigma_w/2S$; —·—, σ_w^3/ϵ; ----, $\eta = (\nu^3/\epsilon)^{\frac{1}{4}}$.

magnitude than the deviation from one found in figure 18*a*.) When the *Re* correction of Perry, Lim & Henbest (1985), Perry, Henbest & Lim (1986) is utilized (i.e. σ_w^2 is replaced by $\sigma_w^2 + C_1'(\nu\epsilon)^{\frac{1}{2}}$ and q^2 by $q^2 + 3C_1'(\nu\epsilon)^{\frac{1}{2}}$, with C_1' taken to be 2.8, after Spalart 1988), both $\epsilon l_{\mathrm{HSB}}/\sigma_w^3$ and $\epsilon L_{\mathrm{BW}}/C_\epsilon q^3$ become less than one. The adjusted predictions are given by the solid curves in figure 18(*a*). The original and modified versions of the Brost model are of comparable accuracy, but the *Re* correction significantly improves the Hunt parameterization. Both adjusted schemes are most accurate in the $0.2h < z < 0.6h$ region, where the flow is most strongly turbulent (figure 9*b*).

Using a value of C_1' less than 2.8 improves both models. With $C_1' = 1.7$, the adjusted $\epsilon L_{\mathrm{BW}}/C_\epsilon q^3$ and especially $\epsilon l_{\mathrm{HSB}}/\sigma_w^3$ (because of the dominant role of z^{-1}, the Brost model is less sensitive to the Perry *Re* correction) become very close to 1.0. The value of C_1' has yet to be agreed upon. Spalart's (1988) value of 2.8 is lower than the 3.8 originally proposed by Perry *et al.* (1985). A further reduction may be required.

Mason & Derbyshire (1990) also found the Brost and Hunt schemes to be of comparable accuracy. It appears as if the concepts behind both dissipation closures are sound. As shown by the lengthscale profiles in figure 18(*b*), q^3/ϵ is roughly proportional to σ_w/N, and σ_w^3/ϵ to $\sigma_w/2S$. There are two aspects of the Brost model, however, that justify a slight preference for the Hunt model. The first (also pointed out by Mason & Derbyshire 1990) is that blocking is significant far from the surface, where the effects of stratification should be dominant (compare figures 18*a* and 8*a*). This seems to be inconsistent with the local scaling concept upon which the model is based. The second concern has to do with the use of q^3, instead of σ_w^3, to represent the dissipation. Horizontal velocity fluctuations (and therefore q) in boundary layers often contain contributions from 'inactive motions' that are unrelated to ϵ (Bradshaw 1967). In contrast, σ_w tends to be a universal function of u_* (Townsend 1976). Therefore σ_w^3/l should be a better measure of the dissipation, and is recommended over q^3/l. But since the Brost parameterization models ϵ using, not the actual value, but a model for q, which may be unaffected by the inactive motions, and since the DNS results provide no basis for preferring one model over the other, these objections are perhaps not important from the user's point of view.

The DNS data were also used to check the performance of gradient closures for the temperature fluctuations and turbulent heat flux. The former (Nieuwstadt 1984; Hunt *et al.* 1985) is

$$\sigma_\Phi = \zeta_\Phi \frac{\sigma_w}{N} \frac{\mathrm{d}\langle \Phi \rangle}{\mathrm{d}z}, \tag{14}$$

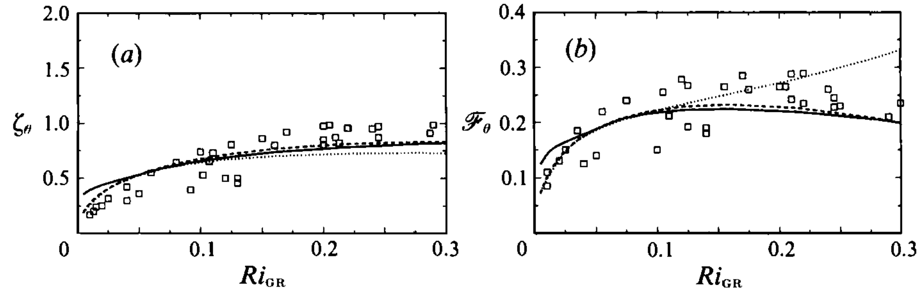

FIGURE 19. Closure parameters for (*a*) temperature variance (equation (14)) and (*b*) heat flux (equation (15)) given by Case SA (time averaged): —, DNS; □, Mason & Derbyshire's (1990) LES results; ----, equations (16) and (17); ···, Brost & Wyngaard's (1978) second-order model.

and the latter,
$$-\langle w'\Phi'\rangle = \mathscr{F}_\Phi \frac{\sigma_w^2}{N}\frac{\mathrm{d}\langle\Phi\rangle}{\mathrm{d}z}, \tag{15}$$

where ζ_Φ is a constant of order 1, and $\mathscr{F}_\Phi$ a thermal diffusivity parameter much smaller than one (Hunt *et al.* 1985).

The buoyancy scale σ_w/N figures prominently in both (14) and (15). In fact, the temperature variance parameter ζ_Φ can be interpreted as the ratio of the thermal lengthscale, $\sigma_\phi/(\mathrm{d}\langle\Phi\rangle/\mathrm{d}z)$, and σ_w/N. The ratio is plotted in figure 19(*a*) versus the gradient Richardson number to allow comparison with results from Mason & Derbyshire's (1990) LES study (symbols) and Brost & Wyngaard's (1978) second-order model (dotted curve) applied 'diagnostically' (see CFS*b*). In accordance with local scaling, data from all three sources (DNS, LES, and second-order model) collapse fairly well when plotted against Ri_{GR}. (By assuming all quantities – including Ri_{GR} – monotonically depend only on z/Λ, local scaling implies that they are unique functions of Ri_{GR}). Based on atmospheric measurements Nieuwstadt (1984) and Hunt *et al.* (1985) found ζ_Φ to be about 0.96 (at $Ri_{\mathrm{GR}} \approx 0.2$) and 0.8, respectively. Both values are only slightly larger than the DNS results near $Ri_{\mathrm{GR}} = 0.2$, the Richardson number typical of atmospheric conditions (Mahrt *et al.* 1979; Nieuwstadt 1984, 1985).

Assuming that the turbulent thermal diffusivity is proportional to the product of a single length and velocity scale, and further assuming the scales are σ_w/N and σ_w, respectively, leads to the expression (15). The thermal diffusivity parameter, $\mathscr{F}_\Phi$, associated with this closure has been measured by Nieuwstadt (1984) as 0.25, and by Hunt *et al.* (1985) as 0.17. The behaviour of $\mathscr{F}_\Phi$ found in the DNS and Mason & Derbyshire's LES data, and the (diagnostic) prediction of Brost & Wyngaard's model (see CFS*b*) are shown in figure 19(*b*). The Case SA, LES and second-order model results are comparable to Nieuwstadt's and Hunt *et al.*'s values. For $Ri_{\mathrm{GR}} < 0.15$, all the data point to a unique dependence on gradient Richardson number. Above $Ri_{\mathrm{GR}} = 0.15$, the DNS and LES results decrease slightly with increasing Ri_{GR}, while Brost & Wyngaard's $\mathscr{F}_\Phi$ does not.

The agreement of the dependence of ζ_Φ and $\mathscr{F}_\Phi$ on Ri_{GR} between the DNS and LES results (that have quite different Richardson number profiles), besides validating local scaling, implies that the temperature variance and heat flux can be accurately represented by the simple closures of (14) and (15). The correspondence between the (low-*Re*) DNS and (high-*Re*) LES results also shows that the behaviour of the heat flux and temperature fluctuations is relatively insensitive to Reynolds number.

A curve fit of the DNS data for the equation (14) and (15) parameters, which incorporates the expected $Ri_{\mathrm{GR}}^{\frac{1}{2}}$ behaviour as $Ri_{\mathrm{GR}} \rightarrow 0$ (inferred by considering the $g/T_{\infty} \rightarrow 0$ limit), produces the following expressions:

$$\zeta_{\Phi} = 3.00\, Ri_{\mathrm{GR}}^{\frac{1}{2}} - 2.70\, Ri_{\mathrm{GR}}, \tag{16}$$

$$\mathscr{F}_{\Phi} = 1.17\, Ri_{\mathrm{GR}}^{\frac{1}{2}} - 1.47\, Ri_{\mathrm{GR}}. \tag{17}$$

These interpolants, shown as dashed curves in figure 19, should be used only for $0 \leqslant Ri_{\mathrm{GR}} \leqslant 0.3$.

6. Results: Cases SB, SC and SD ($a_* \leqslant 5D$)

To this point, the only stable flow discussed was produced by superimposing a temperature profile with relatively large a_*/D on a neutral field. The parameter a_*/D determines the 'elbow' or elevation at which $\Gamma = 0.01\Gamma_0$, marking the transition from neutral to stable stratification. In Case SA, it is in the irrotational region of the initial flow. To be precise, in Case SA $a_* = 0.42 z_{\mathrm{max}} = 1.3\ (h_{\mathrm{S}})_{\mathrm{IC}}$, where $(h_{\mathrm{S}})_{\mathrm{IC}}$ is the 5% shear height of the initial neutral layer. As we have seen, the turbulence quickly adjusts to the imposed stratification, producing a flow representative of the weakly stratified late-night boundary layer.

Three simulations have been performed, with $a_*/D \leqslant 5$, typical of earlier evening nocturnal layers. In all cases, a_* lies within the vortical portion of the initial flow, with either $a_*/D = 5$ (Case SB) or $a_*/D = 0.75$ (SC and SD); see table 1. The former and latter correspond, respectively, to $a_*/z_{\mathrm{max}} = 0.21$ and 0.03, $a_*/(h_{\mathrm{S}})_{\mathrm{IC}} = 0.7$ and 0.1, and (in viscous units) $a_*^+ = 130$ and 20. The early portions of Cases SC and SD ($a_*/D = 0.75$) are similar to Mason & Derbyshire's (1990) LES runs, which were initialized by reducing the surface temperature (equivalent to choosing $a_* = 0$). Our principal goal in this section is to address the question of how the various initial temperature profiles affect the developed flow state. The answer is found by comparing the mean temperature evolution in figures 3(*a*), 20(*a*), 21(*a*) and 22(*a*), and the variation of Ri_{GR} in figures 8(*a*), 20(*b*), 21(*b*) and 22(*b*). The early-time portions of the three low-a_* runs (when the upper regions are unstratified) are similar to the flows studied by Mason & Derbyshire, who considered times $\leqslant 0.7/f$. As the layer changes from early evening to late night conditions, the effect of buoyancy propagates upward in Cases SB and SD, until the turbulence in the uppermost elevations is diminished (where $Ri_{\mathrm{GR}} \gg 0.25$; figures 20b and 22b). The transition from the early state, where $\mathrm{d}Ri_{\mathrm{GR}}/\mathrm{d}z \approx 0$ in the outer layer, to the final configuration, with $Ri_{\mathrm{GR}} \rightarrow \infty$ as $z \rightarrow \infty$, is relatively quick, due to the low Reynolds number of the flow. Comparing Cases SB, SC and SD, we see that the weaker the stratification (in terms of the total temperature difference across the layer, which is a function of both $Ri_{0,0}$ and a_*) the higher it must propagate to be felt, and the thicker the remaining turbulent layer, as shown by the respective heights at which Ri_{GR} becomes large (note that the vertical axis scale in figure 8*a* differs from that in figures 20*b*, 21*b* and 22*b*). For Case SC, the surface-to-free-stream temperature difference is so small that even in the outer layer the buoyancy has only a minor effect upon the turbulence, and Ri_{GR} remains less than 0.25. The final stages of the other two low-a_* runs have Richardson number profiles qualitatively similar to that of Case SA (cf. figure 8*a*). Coupled with the earlier observation that the turbulence quickly equilibrates with the local conditions, this is further evidence that the temperature initialization has not adversely affected the results presented in the previous section.

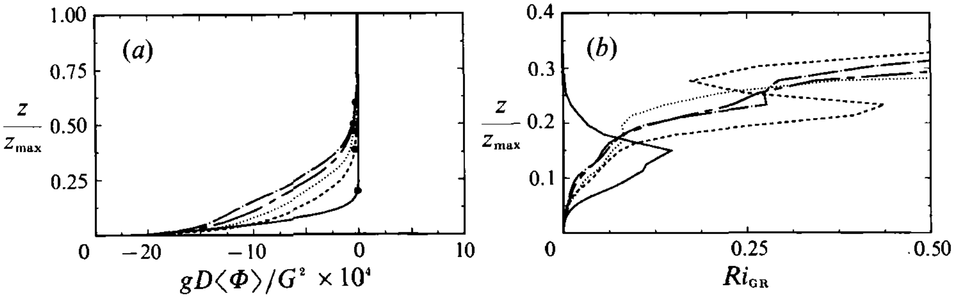

FIGURE 20. Profiles for Case SB ($a_*/D = 5$, $Ri_{0,0} = 0.001$): —, $tf = 0$ (initial condition); ----, $tf = 1.1$; · · ·, $tf = 2.2$; ———, $tf = 3.4$; — · —, $tf = 4.5$. (a) Mean temperature (● marks elevation at which $\Gamma/\Gamma_0 = 0.01$), and (b) gradient Richardson number.

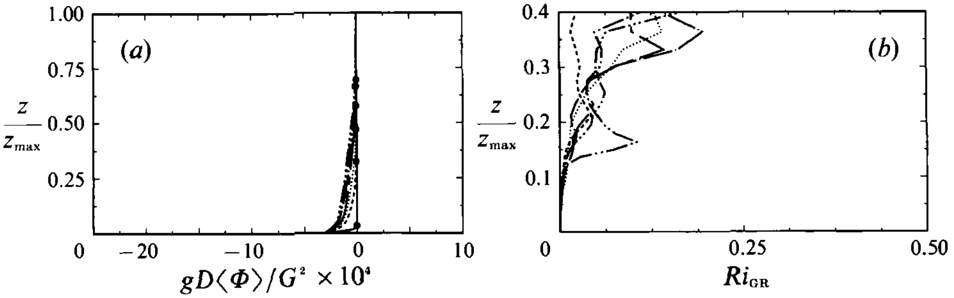

FIGURE 21. Profiles for Case SC ($a_*/D = 0.75$, $Ri_{0,0} = 0.001$) (a) Mean temperature and (b) gradient Richardson number. ($Ri_{GR} \approx 0$ at $tf = 0$.) Symbols as figure 20, with — · · —, $tf = 5.7$; — · · · —, $tf = 6.9$.

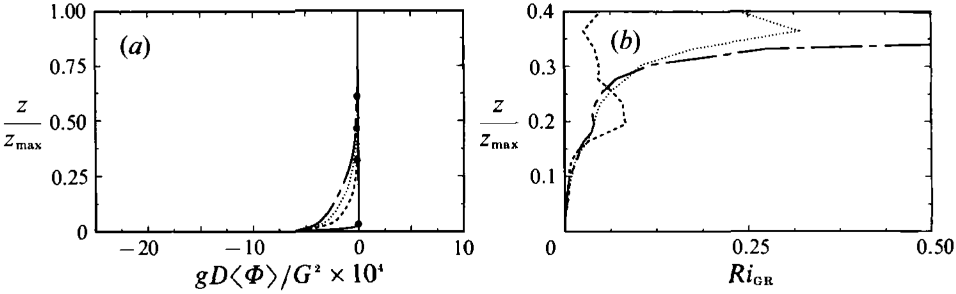

FIGURE 22. Profiles for Case SD ($a_*/D = 0.75$, $Ri_{0,0} = 0.002$). (a) Mean temperature and (b) gradient Richardson number. ($Ri_{GR} \approx 0$ at $tf = 0$.) Symbols as figure 20.

7. Discussion and conclusions

7.1 *Flow structure*

Stable stratification has a significant effect on turbulence. It is well known that the largest vertical scales are most strongly influenced by buoyancy (Wyngaard 1982, p. 74). For the Ekman layer this means (for cases in which the stratification is not so strong as to completely extinguish the turbulence) that the greatest difference between the neutral and stratified flows occurs in the outer region, where the scales are largest and the shear weakest. Thus, the outer-layer fluxes are diminished (figure 8c), and the thickness of the turbulent layer is reduced, but the properties of the near-surface eddies remain about the same (see figure 6). Consequently, the major difference between the stratified and unstratified surface stresses is not in magnitude but in direction; the surface shear angle β is larger in the stratified layer, because there is more turning of the mean velocity in the outer region. Near the surface, the effects are more subtle. Buoyancy reduces both the turbulent kinetic energy (figure 5*a*) and the Reynolds shear stress (figure 4), the latter more than the former (figure 12). By reducing the thickness of the turbulent layer, the stratification also increases the shear in most of the layer (figure 15) (very near the surface the slightly weaker Reynolds stresses lead to a smaller surface velocity gradient; see figure 2*c* and table 3.) Thus the eddy viscosity is greatly diminished by stratification (figure 14). All of these changes are greater than is implied by a direct measure of the relative strength of the buoyancy. For example, the stratification is never directly responsible for more than 20% of the rate of destruction of the turbulent kinetic energy in Case SA (figure 8*a*, *b*). This extra destruction is not enough to explain the magnitude of the observed change of the rate of growth of $\frac{1}{2}q^2$. The direct reduction in the growth rate of the integrated turbulent kinetic energy E caused by the buoyancy is

$$g\int_0^\infty \langle w'\Phi'\rangle \,\mathrm{d}z.$$

Assuming a linear distribution for $\langle w'T'\rangle$ (see figure 11*a*), this reduction can be estimated as

$$\mathrm{d}(E/DG^2)/\mathrm{d}(tf) \approx -\tfrac{1}{2}(Ri_0/RePr)(Gh/fD^2).$$

For the buoyancy to directly produce the 40% reduction in E found for Case SA (for which $Gh/fD^2 = 1400$) would therefore require a time of $tf \approx 8.5$, instead of the $tf \approx 0.5$ observed in figure 2*b*. Physically, the stratification reduces the intensity and scale of the vertical motions and thereby the vertical transport of momentum (Reynolds shear stress) that in turn diminishes the rate of production of turbulent energy (cf. figure 15*b*). (There is also a reduction in the rate of viscous dissipation (implied by the vorticity evolution in figure 5*b*) but it is not as great as the production rate decrease.) Since the indirect effect of the buoyancy is much stronger than the direct effect, stable stratification may be considered as a type of 'extra-strain', similar to, for example, rotation (Bradshaw 1973; CFS*a*).

The stratification also influences the horizontal scales; there is a correlation between the Richardson number and whether the buoyancy causes an increase or decrease of the streamwise integral scale (see §§5.2, 5.3.2).

For the cases in which the stratification eliminates all the turbulence (presented in CFS*b*), evidence of gravity-induced reconversion of potential to kinetic energy was found. This process is marked by the presence of a counter-gradient heat flux (Schumann 1987; see Gerz *et al.* 1989 and Holt *et al.* 1992 for alternative physical explanations of the counter-gradient flux). The collapsed turbulent state is the only one that contained significant wave-like motions. When the turbulence is three-dimensional (Cases SA, SB, SC and SD), the lack of complicated topography and stratification aloft (and possibly low Reynolds number) here precludes the existence of buoyant oscillations in the outer region. Near the surface, where Γ is large and waves could presumably be superimposed upon the turbulence, little difference was found between the stable and neutral layers (see CFS*b*).

7.2. *Reynolds-averaged closures*

Both the 'constant Froude number' (Brost & Wyngaard 1978, and equation (11)) and 'shearing lengthscale' (Hunt *et al.* 1988, and equation (13)) approaches to parameterizing the dissipation were generally successful when corrected for the low

Reynolds number of the simulation (figure 18*a*). For the flow considered here, both the buoyancy and shearing lengthscales adequately capture the behaviour of the dissipation.

Simple gradient closures for the temperature variance (14) and heat flux (15) were also found to be valid, in that the variation of the parameters for each (ζ_Φ and $\mathscr{F}_\Phi$) depends simply on the gradient Richardson number, confirming the finding of Mason & Derbyshire (1990). The similarity of DNS and LES results implies that the heat flux and temperature fluctuations are relatively insensitive to Reynolds number.

Our computations also provide support for the concept of local scaling, which indirectly supports the assumptions (e.g. that the third-order moments (cf. figure 8*c*) and time-rate-of-change of the second-order moments are negligible) used in the full Brost–Wyngaard second-order model. Given the low Reynolds number and mild stratification, the correspondence of the simulation results with atmospheric data is quite striking (see figure 17*a*, *b*). Although the agreement of the profiles for temperature variance and eddy viscosity is less satisfactory (figure 17*c*, *d*) part of the disparity may be due to uncertainty in the field data. The fact that the discrepancy in the temperature variance is much less when the effect of internal waves upon the atmospheric data is accounted for, and the similar variation of the temperature variance closure parameter with Ri_{GR} in both the DNS and Mason & Derbyshire's LES results provides some support for this possibility.

The general agreement between the results of this study and Mason & Derbyshire's implies that the stable Ekman layer can be accurately computed using LES. It also demonstrates that information generated by DNS can, in some instances, be applied to high-Reynolds-number atmospheric flows.

This work has been sponsored by the Office of Naval Research under contract N00014-86-K-0157. Computer resources have been furnished by the Central Computer Facility at NASA Ames Research Center. Thanks are due to Ms D. M. Bell, Drs W. M. Chan, S. E. Holt, S. G. Monismith, R. D. Moser, K. R. Shariff, D. D. Stretch and A. A. Wray for their input. We are also grateful for the helpful suggestions supplied by Dr M. M. Rogers, for the careful reading and comments given by the reviewers, and for the guidance provided by Professor R. L. Street.

REFERENCES

ABRAMOWITZ, M. & STEGUN, A. 1972 *Handbook of Mathematical Functions*. National Bureau of Standards.

BLACKADAR, A. K. 1957 Boundary layer wind maxima and their significance for the growth of the nocturnal inversion. *Bull. Am. Met. Soc.* **38**, 283–290.

BRADSHAW, P. 1967 'Inactive' motion and pressure fluctuations in turbulent boundary layers. *J. Fluid Mech.* **30**, 241–258.

BRADSHAW, P. 1973 Effects of streamline curvature on turbulent flow. *AGARD-AG*-169.

BROST, R. A. & WYNGAARD, J. C. 1978 A model study of the stably stratified planetary boundary layer. *J. Atmos. Sci.* **35**, 1427–1440.

BUSINGER, J. A. 1982 Equations and concepts. In *Atmospheric Turbulence and Air Pollution Modelling* (ed. F. T. M. Nieuwstadt & H. Van Dop), Chap. 1. D. Reidel.

COLEMAN, G. N., FERZIGER, J. H. & SPALART, P. R. 1990*a* A numerical study of the turbulent Ekman layer. *J. Fluid Mech.* **213**, 313–348 (referred to herein as CFS*a*).

COLEMAN, G. N., FERZIGER, J. H. & SPALART, P. R. 1990*b* A numerical study of the stratified turbulent Ekman layer. *Dept. of Mech. Engng, Stanford University, Thermosciences Div. Rep. TF*-48 (referred to herein as CFS*b*).

Derbyshire, S. H. 1990 Nieuwstadt's stable boundary layer revisited. *Q. J. R. Met. Soc.* **116**, 127–158.

Ekman, V. W. 1905 On the influence of the Earth's rotation on ocean-currents. *Arkiv Matematic, Astronomi Fysik.* **2**(11), 1–52.

Fitzjarrald, D. E. 1979 On using a simplified turbulence model to calculate eddy diffusivities. *J. Atmos. Sci.* **36**, 1817–1820.

Fleagle, R. G. & Businger, J. A. 1980 *An Introduction to Atmospheric Physics.* Academic.

Garratt, J. R. 1982 Observations in the nocturnal boundary layer. *Boundary-Layer Met.* **22**, 21–48.

Gerz, T., Schumann, U. & Elghobashi, S. E. 1989 Direct numerical simulation of stratified homogeneous turbulent shear flows. *J. Fluid Mech.* **200**, 563–594.

Gill, A. E. 1982 *Atmospheric-Ocean Dynamics.* Academic.

Gottlieb, D. & Orszag, S. A. 1977 *Numerical Analysis of Spectral Methods: Theory and Applications.* Society for Industrial and Applied Mathematics.

Gregg, M. C. 1987 Diapycnal mixing in the thermocline: a review. *J. Geophys. Res.* **92**, 5249–5286.

Holt, S. E., Koseff, J. R. & Ferziger, J. H. 1992 A numerical study of the evolution and structure of homogeneous stably stratified sheared turbulence. *J. Fluid Mech.* **237**, 499–539.

Holton, J. R. 1979 *An Introduction to Dynamic Meteorology.* Academic.

Hunt, J. C. R. 1985 Diffusion in the stably stratified atmospheric boundary layer. *J. Clim. Appl. Met.* **24**, 1187–1195.

Hunt, J. C. R., Kaimal, J. C. & Gaynor, J. E. 1985 Some observations of turbulence structure in stable layers. *Q. J. R. Met. Soc.* **111**, 793–815.

Hunt, J. C. R., Spalart, P. R. & Mansour, N. N. 1987 A general form for the dissipation length scale in turbulent shear flows. *Proc. 1st. Summer Prog.* NASA/Stanford Center for Turbulence Research.

Hunt, J. C. R., Stretch, D. D. & Britter, R. E. 1988 Length scales in stably stratified turbulent flows and their use in turbulence models. In *Stably Stratified Flow and Dense Gas Dispersion* (ed. J. S. Puttock). Clarendon.

Kays, W. M. & Crawford, M. E. 1980 *Convective Heat and Mass Transfer*, 2nd edn. McGraw-Hill.

Kim, J. & Moin, P. 1989 Transport of passive scalars in a turbulent channel flow. In *Turbulent Shear Flows 6* (ed. J.-C. André, J. Cousteix, F. Durst, B. E. Launder, F. W. Schmidt & J. H. Whitelaw). Springer.

Kim, J., Moin, P. & Moser, R. D. 1987 Turbulent statistics in fully developed channel flow at low Reynolds number. *J. Fluid Mech.* **177**, 133–166.

Kraichnan, R. H. 1967 Inertial ranges in two-dimensional turbulence. *Phys. Fluids* **10**, 1417–1423.

Lee, M. J., Kim, J. & Moin, P. 1990 Structure of turbulence at high shear rate. *J. Fluid Mech.* **216**, 561–583.

LeMone, M. A. 1973 The structure and dynamics of horizontal roll vortices in the planetary boundary layer. *J. Atmos. Sci.* **30**, 1077–1091.

Lin, J.-T. & Pao, Y.-H. 1979 Wakes in stratified fluids. *Ann. Rev. Fluid Mech.* **11**, 317–338.

Mahrt, L., Heald, R. C., Lenschow, D. H. & Stankov, B. B. 1979 An observational study of the structure of the nocturnal boundary layer. *Boundary-Layer Met.* **17**, 247–264.

Mason, P. J. & Derbyshire, S. H. 1990 Large eddy simulation of the stably-stratified atmospheric boundary layer. *Boundary-Layer Met.* **53**, 117–162.

Métais, O. & Herring, J. R. 1989 Numerical simulations of freely evolving turbulence in stably stratified fluids. *J. Fluid Mech.* **202**, 117–148.

Nieuwstadt, F. T. M. 1984 The turbulent structure of the stable, nocturnal boundary layer. *J. Atmos. Sci.* **41**, 2202–2216.

Nieuwstadt, F. T. M. 1985 A model for the stationary, stable boundary layer. In *Turbulence and Diffusion in Stable Environments* (ed. J. C. R. Hunt). Clarendon.

Ozmidov, R. V. 1965 On the turbulent exchange in a stably stratified ocean. *Izv. Atoms. Ocean. Phys.* **8**, 853–860.

PERRY, A. E., HENBEST, S. & CHONG, M. S. 1986 A theoretical and experimental study of wall turbulence. *J. Fluid Mech.* **165**, 163–199.

PERRY, A. E., LIM, K. L. & HENBEST, S. M. 1985 A spectral analysis of smooth flat-plate boundary layers. *Proc. 5th Symp. on Turbulent Shear Flows, Ithaca, NY, August 7–9, 1985.*

RILEY, J. J., METCALFE, R. W. & WEISSMAN, M. A. 1981 Direct numerical simulations of homogeneous turbulence in density-stratified fluids. *Proc. AIP Conf. Non-Linear Properties of Internal Waves* (ed. B. J. West), Vol. 76, pp. 79–112.

ROGERS, M. M., MANSOUR, N. N. & REYNOLDS, W. C. 1989 An algebraic model for the turbulent flux of a passive scalar. *J. Fluid Mech.* **203**, 77–101.

SCHMIDT, H. & SCHUMANN, U. 1989 Coherent structure of the convective boundary layer derived from large-eddy simulations. *J. Fluid Mech.* **200**, 511–562.

SCHUMANN, U. 1987 The countergradient heat flux in turbulent stratified flows. *Nucl. Engng Des.* **100**, 255–262.

SORBJAN, Z. 1986 On similarity in the atmospheric boundary layer. *Boundary-Layer Met.* **34**, 377–397.

SPALART, P. R. 1988 Direct simulation of a turbulent boundary layer up to $R_\theta = 1410$. *J. Fluid Mech.* **187**, 61–98.

SPALART, P. R. 1989 Theoretical and numerical study of a three-dimensional turbulent boundary layer. *J. Fluid Mech.* **205**, 319–340.

SPALART, P. R., MOSER, R. D. & ROGERS, M. M. 1991 Spectral methods for the Navier–Stokes equations with one infinite and two periodic directions. *J. Comp. Phys.* **96**, 297–324.

STILLINGER D. C., HELLAND, K. N. & VAN ATTA, C. W. 1983 Experiments on the transition of homogeneous turbulence to internal waves in a stratified fluid. *J. Fluid Mech.* **131**, 91–122.

STULL, R. B. 1988 *An Introduction to Boundary Layer Meteorology.* Kluwer.

THORPE, A. J. & GUYMER, T. H. 1977 The nocturnal jet. *Q. J. R. Met. Soc.* **103**, 633–653.

TOWNSEND, A. A. 1976 *The Structure of Turbulent Shear Flow.* Cambridge University Press.

TURNER, J. S. 1973 *Buoyancy Effects in Fluids.* Cambridge University Press.

WYNGAARD, J. C. 1973 On surface layer similarity. In *Workshop on Micrometeorology* (ed. D. A. Haugen), Chap. 3. American Meteorological Society.

WYNGAARD, J. C. 1982 Boundary layer modeling. In *Atmospheric Turbulence and Air Pollution Modelling* (ed. F. T. M. Nieuwstadt & H. Van Dop), Chap. 1. D. Reidel.

WYNGAARD, J. C. 1983 Lectures on the planetary boundary layer. In *Mesoscale Meteorology – Theories, Observations and Models* (ed. D. K. Lilly & T. Gal-Chen). D. Reidel.

WYNGAARD, J. C. 1985 Structure of the planetary boundary layer and implications for its modeling. *J. Clim. Appl. Met.* **24**, 1131–1142.

WYNGAARD, J. C. 1992 Atmospheric turbulence. *Ann. Rev. Fluid Mech.* **24**, 205–233.

ZILITINKEVICH, S. S. 1972 On the determination of the height of the Ekman boundary layer. *Boundary-Layer Met.* **3**, 141–145.

ZILITINKEVICH, S. S. 1975 Resistance laws and prediction equations for the depth of the planetary boundary layer. *J. Atmos. Sci.* **32**, 743–752.